Estimating Emissions of Methane Consistent with Atmospheric Measurements of Methane and δ^{13}C of Methane

Sourish Basu[1,2], Xin Lan[3,4], Edward Dlugokencky[4], Sylvia Michel[5], Stefan Schwietzke[6], John B. Miller[4], Lori Bruhwiler[4], Youmi Oh[4], Pieter P. Tans[4], Francesco Apadula[7], Luciana V. Gatti[8], Armin Jordan[9], Jaroslaw Necki[10], Motoki Sasakawa[11], Shinji Morimoto[12], Tatiana Di Iorio[13], Haeyoung Lee[14], Jgor Arduini[15], and Giovanni Manca[16]

[1]Global Modeling and Assimilation Office, NASA Goddard Space Flight Center, Greenbelt MD
[2]Earth System Science Interdisciplinary Center, University of Maryland, College Park MD
[3]Cooperative Institute for Research in Environmental Science, University of Colorado, Boulder CO
[4]Global Monitoring Laboratory, National Oceanic and Atmospheric Administration, Boulder CO
[5]Institute for Arctic and Alpine Research, University of Colorado, Boulder CO
[6]Environmental Defense Fund, Berlin, Germany
[7]Ricerca sul Sistema Energetico (RSE S.p.A.), Milano, Italy
[8]Instituto Nacional de Pesquisas Espaciais, São José dos Campos, São Paulo, Brazil
[9]Max Planck Institute for Biogeochemistry, Jena, Germany
[10]AGH University of Science and Technology, Krakow, Poland
[11]National Institute for Environmental Studies, Tsukuba-shi, Ibaraki, Japan
[12]Center for Atmospheric and Oceanic Studies, Tohoku University, Sendai, Japan
[13]Italian National Agency for New Technologies, Energy, and Sustainable Economic Devlopment (ENEA), Rome, Italy
[14]National Institute of Meteorological Sciences, Seogwipo-si, Jeju-do, Korea
[15]Università degli Studi di Urbino, Urbino, Italy
[16]European Commission, Joint Research Center, Ispra, Italy

Correspondence: Sourish Basu (sourish@umd.edu)

Abstract. We have constructed an atmospheric inversion framework based on TM5 4DVAR to jointly assimilate measurements of methane and δ^{13}C of methane in order to estimate source-specific methane emissions. Here we present global emission estimates from this framework for the period 1999–2016. We assimilate a newly constructed, multi-agency database of CH_4 and $\delta^{13}CH_4$ measurements. We find that traditional CH_4-only atmospheric inversions are unlikely to estimate emissions consistent with atmospheric $\delta^{13}CH_4$ data, and assimilating $\delta^{13}CH_4$ data is necessary to deriving emissions consistent with both measurements. Our framework attributes *ca.* 85% of the post-2007 growth in atmospheric methane to microbial sources, with about half of that coming from the Tropics between 23.5 °N and 23.5 °S. This contradicts the attribution of the recent growth in the methane budget of the Global Carbon Project (GCP). We find that the GCP attribution is only consistent with our top-down estimate in the absence of $\delta^{13}CH_4$ data. We find that at global and continental scales, $\delta^{13}CH_4$ data can separate microbial from fossil methane emissions much better than CH_4 data alone can, and at smaller scales this ability is limited by the current $\delta^{13}CH_4$ measurement coverage. Finally, we find that the largest uncertainty in using $\delta^{13}CH_4$ data to separate different methane source types comes from our knowledge of atmospheric chemistry, specifically the distribution of tropospheric chlorine and the isotopic discrimination of the methane sink.

1 Introduction

Current atmospheric levels of methane (CH_4) are about 2.5 times pre-industrial levels, primarily due to anthropogenic emissions (Dlugokencky et al., 2011). The main sources of CH_4 to the atmosphere today are known, which are periodically summarized by the Global Carbon Project (GCP, Saunois et al., 2020). In brief, they include anthropogenic sources from agriculture (ruminants, manure, and rice), waste management (landfills and waste treatment), fossil fuel production and use (coal, oil, and natural gas), and biomass burning (including biofuels). The remainder is from natural processes, predominantly tropical and high northern latitude wetlands, with smaller contributions from termites, wild animals and geologic seeps. In the latest GCP report, however, there remains a large disparity of $\sim 160\,\mathrm{Tg\,yr^{-1}}$ between the bottom-up budget constructed from inventories and the top-down budget derived from atmospheric CH_4 measurements (Saunois et al., 2020), signifying gaps in our understanding of the CH_4 budget.

As shown in Figure 1, CH_4 levels have been rising rapidly since 2007 after a period of relatively slow growth in 1999–2006 (Dlugokencky et al., 2011; Saunois et al., 2020). The mechanisms behind the relative stability of 1999–2006 and growth thereafter, however, are not yet fully understood. Possible mechanisms suggested in the literature include an approach to a steady state in the early 2000s (Dlugokencky et al., 2003) followed by an increase in either agricultural (Schaefer et al., 2016) or fossil (Worden et al., 2017) emissions, or both (Saunois et al., 2020; Jackson et al., 2020); increase in global (Schwietzke et al., 2016) or tropical (Nisbet et al., 2016, 2019) microbial emissions; a decrease in methane uptake by upland soils (Ni and Groffman, 2018); and decadal changes in the atmospheric sinks of methane (Rigby et al., 2017; Turner et al., 2017). It is difficult to choose between these competing explanations based on atmospheric CH_4 measurements alone. However, measurements of the $^{13}C{:}^{12}C$ ratio of CH_4, denoted $\delta^{13}C-CH_4$ or $\delta^{13}CH_4$ in short, provide some additional information to distinguish between these hypotheses (Lan et al., 2021).

Different CH_4 sources have distinct $\delta^{13}CH_4$ signatures over large spatial scales, and different sinks consume $^{12}CH_4$ and $^{13}CH_4$ at slightly different rates, imposing different signals on atmospheric $\delta^{13}CH_4$ (Miller, 2004). Therefore, atmospheric $\delta^{13}CH_4$ measurements can help constrain and refine the CH_4 budget. In an earlier publication, we described the simulation of atmospheric CH_4 and $\delta^{13}CH_4$ using the model TM5 (Krol et al., 2005) and its use for evaluating competing hypotheses about renewed CH_4 growth since 2007 (Lan et al., 2021). In this work, we construct and apply a variational inversion framework based on TM5 to assimilate CH_4 and $\delta^{13}CH_4$ measurements and estimate space- and time-varying emissions of CH_4 disaggregated by source type. With this framework, we perform atmospheric inversions from 1997 to 2016 to infer large scale methane emissions from different sources, assess the added value of $\delta^{13}CH_4$ measurements compared to traditional CH_4-only inversions, and investigate the possible factors behind the post-2007 growth in atmospheric CH_4.

Several previous studies have used the information provided by $\delta^{13}CH_4$ measurements to infer mechanisms behind the behavior of atmospheric methane over the past two decades. However, many of these studies approximated the global atmosphere as a small number of connected boxes, with homogeneous emissions and chemistry in each box (e.g., Schwietzke et al., 2016; Schaefer et al., 2016; Nisbet et al., 2016, 2019; Worden et al., 2017; Zhang et al., 2021b). They were therefore susceptible to biases inherent in box models (Naus et al., 2019) and were unable to use the information contained in spatial gradients

of atmospheric CH_4 and $\delta^{13}CH_4$. Moreover, by construction, box models have to simplify the complexity of $\delta^{13}CH_4$ source signatures, transport variability and loss processes, and cannot extract information from spatial gradients in atmospheric measurements. In § 4.3, we explore some of the limitations of box models and their differences from a 3D model by comparing our conclusions to those from the recently published work of Zhang et al. (2021b), which used a box model in combination with atmospheric CH_4 and $\delta^{13}CH_4$ data to infer causes behind the post-2007 growth in atmospheric CH_4. Some studies have used 3D atmospheric circulation models to estimate CH_4 emissions consistent with observed $\delta^{13}CH_4$ (e.g., Bousquet et al., 2006; Rice et al., 2016). However, they have generally used globally uniform $\delta^{13}CH_4$ source signatures, when in reality signatures of some of the most important sources such as wetlands and fossil fuels have strong latitudinal gradients and spatial variations. In this study, we confront our best estimate of spatio-temporally varying methane emissions and source signatures with a newly constructed multi-laboratory dataset of atmospheric CH_4 and $\delta^{13}CH_4$ measurements in the TM5 4DVAR framework. Our technique is analogous to a recently submitted manuscript by Thanwerdas et al. (2021), and in § 4.4 we discuss the similarities and differences between our methods.

2 Method

2.1 Formulation of the mass balance equations

The atmospheric mass balance of $^{12}CH_4$ can be written as

$$\frac{d}{dt}\,^{12}C = \sum_s {}^{12}F_s - \sum_l {}^{12}k_l \times {}^{12}C \times [l]$$

$$= \sum_s {}^{12}F_s - {}^{12}C \sum_l L_l \tag{1}$$

where F_s denotes the surface flux from source category s, and l denotes species contributing to chemical loss, namely Cl, OH and $O(^1D)$. We classify all sources into three isotopically distinct source categories, namely pyrogenic, fossil and microbial CH_4. While the upland soil sink of methane is included in the sources in conventional methane modeling, for reasons described in § 2.4 we have modeled it as a fourth loss mechanism. The combination $^{12}k_l \times [l]$ can be denoted as a loss rate or inverse lifetime L_l due to species l. For $^{13}CH_4$, we can write a corresponding equation,

$$\frac{d}{dt}\,^{13}C = \sum_s {}^{13}F_s - {}^{13}C \sum_l \alpha_l L_l$$
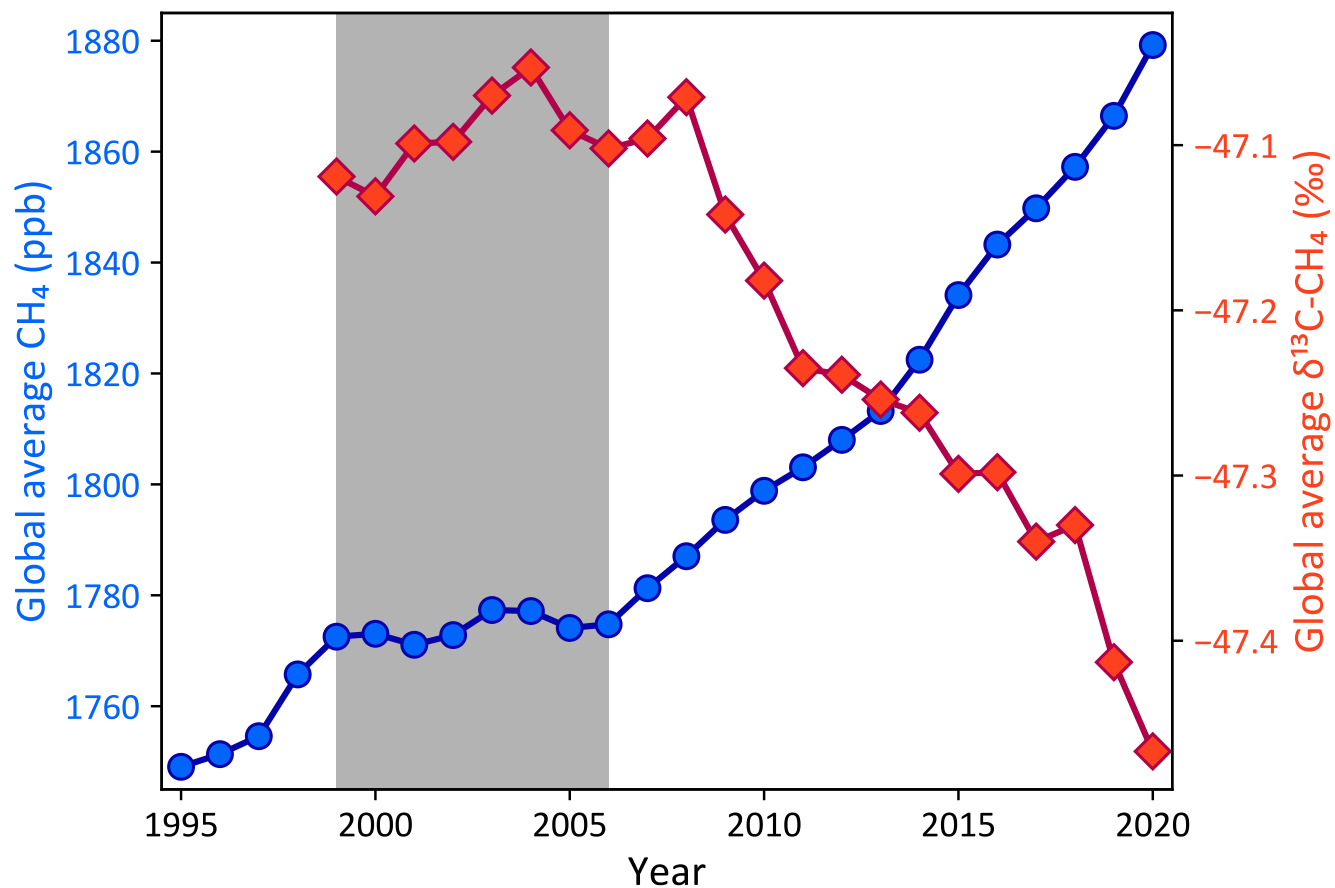
Figure 1. Global average CH_4 (blue circles, left axis) and $\delta^{13}CH_4$ (red diamonds, right axis) from NOAA marine boundary layer (MBL) and other background sampling sites. The gray box denotes the period from 1999 to 2006 when the atmospheric CH_4 burden was relatively stable, in contrast to the periods of growth before and after. Regular $\delta^{13}CH_4$ measurements started at NOAA background sites in 1998, which is the first year with an estimate of the global $\delta^{13}CH_4$. The selection of marine boundary layer sites and the construction of global averages is described in detail by Masarie and Tans (1995).

75

$$\frac{d}{dt}{}^{13}C = \sum_s {}^{13}F_s - {}^{13}C \sum_l \alpha_l L_l \tag{2}$$

where $\alpha_l = {}^{13}k_l/{}^{12}k_l$. Using the definition of δ, we can substitute ${}^{13}C = {}^{12}Cr_{\rm std}(\delta_a+1)$ and ${}^{13}F = {}^{12}Fr_{\rm std}(\delta_s+1)$ and get

$$^{12}C\frac{d}{dt}\delta_a = \sum_s (\delta_s - \delta_a){}^{12}F_s - {}^{12}C(\delta_a + 1)\sum_l \epsilon_l L_l$$

80    ${}^{13}F = {}^{12}Fr_{\rm std}(\delta_s+1)$ and get

$$^{12}C\frac{d}{dt}\delta_a = \sum_s (\delta_s - \delta_a){}^{12}F_s - {}^{12}C(\delta_a + 1)\sum_l \epsilon_l L_l \tag{3}$$

where $\epsilon_l = \alpha_l - 1$ and $r_{\rm std} = 0.0112372$ is a pre-defined standard ratio[1] (Craig, 1957). While equations (1) and (3) are mathematically complete descriptions of the ${}^{12}CH_4$ and ${}^{13}CH_4$ budgets, they are not the most convenient form for constructing a dual tracer CH_4 and $\delta^{13}CH_4$ inversion. This is because it is total CH_4 that is measured and not the two isotopologues separately.

85   We therefore construct an alternate formulation in terms of $\delta' = ({}^{13}CH_4/CH_4)/r_{\rm std} - 1$, which can be related to the more traditional $\delta = ({}^{13}CH_4/{}^{12}CH_4)/r_{\rm std} - 1$ by

$$\delta' = \frac{1+\delta}{1 + r_{\rm std}(1+\delta)} - 1 \tag{4}$$

$$\delta = \frac{1+\delta'}{1 - r_{\rm std}(1+\delta')} - 1 \tag{5}$$

In terms of this δ', the mass balance equations become

90
$$\frac{d}{dt}C = \sum_s F_s - C\sum_l L_l + r_{\rm std}C(\delta_a'+1)\sum_l L_l(1-\alpha_l) \tag{6}$$

$$\frac{d}{dt}C\delta_a' = \sum_s \delta_s' F_s - C\delta_a'\sum_l \alpha_l L_l + C\sum_l L_l(1-\alpha_l) - r_{\rm std}C(\delta_a'+1)\sum_l L_l(1-\alpha_l) \tag{7}$$

where $C = {}^{12}CH_4 + {}^{13}CH_4$ and $F_s = {}^{12}F_s + {}^{13}F_s$ are total methane moles and fluxes respectively. This reformulation of ${}^{13}CH_4$ abundance in terms of total carbon is similar to that by Tans et al. (1993). In eq (6), if we consider the coefficients of any L_l, then the second term supplies $C \sim 1800\,{\rm ppb}$, while the third term supplies $r_{\rm std}C(\delta_a'+1)(1-\alpha_l) \sim$
95    $0.086\,{\rm ppb}$, approximating $r_{\rm std} = 0.01$, $\delta_a' = -0.05$ and $\alpha_l = 0.995$. In eq (7), with the same approximations, the coefficients of L_l in the last three terms are, respectively, $89.5\,{\rm ppb}$, $9\,{\rm ppb}$ and $0.086\,{\rm ppb}$. So in both equations, we ignore $r_{\rm std}C(\delta_a' +$

---

[1]There is not a single unique value of $r_{\rm std}$ in literature. Currently, $r_{\rm std} = 0.011180$ (Zhang and Li, 1990) is used by most measurement laboratories, while values of 0.011117 (Malinovsky et al., 2019) and 0.011125 (Fleisher et al., 2021) have also been reported recently. However, the true value of $r_{\rm std}$ impacts neither our formulation nor our results, as long as a single value is used consistently.

1) $\sum_l L_l(1 - \alpha_l)$, leading to

$$\frac{d}{dt}C \simeq \sum_s F_s - C\sum_l L_l \tag{8}$$

$$\frac{d}{dt}C\delta_a' \simeq \sum_s \delta_s' F_s - C\delta_a' \sum_l \alpha_l L_l + C\sum_l L_l(1 - \alpha_l) \tag{9}$$

In this formulation, the two tracers to be simulated are total CH_4 (which is measured) and an artificial tracer $C\delta_a'$. All measurements of $\delta^{13}CH_4$ are converted to δ_a' before assimilation. Note that the tracer $C\delta_a'$ does not have any surface flux of its own. There is "production" at the surface proportional to the the CH_4 surface flux, and loss in the atmosphere. The loss reactions of eq (8) and (9) are coupled, and the loss of the tracers from time t to $t + \delta t$ is calculated by solving the differential equation to give

$$C(t + \delta t) = C(t)e^{-\delta t \sum_l L_l} \tag{10}$$

$$C\delta'(t + \delta t) = [C(t) + C\delta'(t)]e^{-\delta t \sum_l \alpha_l L_l} - C(t)e^{-\delta t \sum_l L_l} \tag{11}$$

2.2 Inversion framework

We use the TM5 4DVAR inversion framework (Meirink et al., 2008), which has been used to estimate surface fluxes of CO, CO_2 and CH_4 (Hooghiemstra et al., 2011; Bergamaschi et al., 2013; Krol et al., 2013; Basu et al., 2013, 2014) in single-tracer inversions, as well as source-specific CO_2 fluxes in multi-tracer inversions (Basu et al., 2020, 2016; Ma et al., 2021). At the heart of the framework is the TM5 offline tracer transport model (Krol et al., 2005) and its adjoint, driven by ECMWF ERA Interim reanalysis winds and run globally at $3° \times 2°$ with 25 vertical layers defined by sigma-pressure hybrid coordinates. Two tracers are simulated in TM5, total methane or C of eq (8), and the artificial tracer $C\delta_a'$ of eq (9). Measurements of CH_4 are directly compared to modeled values of C, while measurements of $\delta^{13}CH_4$ are first converted to δ_a' and then to $C\delta_a'$ by multiplying with values of CH_4 mole fractions measured in the same air samples.

TM5 4DVAR minimizes a cost-function J as a function of surface fluxes x (the set of all F_s of § 2.1) by balancing fits to atmospheric observations y with deviations from the prior fluxes x_0,

$$J(x) = \frac{1}{2}(Hx - y)^T R^{-1}(Hx - y) + \frac{1}{2}(x - x_0)B^{-1}(x - x_0) \tag{12}$$

where H is the transport, chemistry and observation operator connecting surface fluxes with atmospheric measurements, and R and B are the error covariances of $Hx - y$ and prior fluxes respectively. Our formulation of R contains both the analytical measurement uncertainty and a model representativeness error proportional to local tracer gradients (Meirink et al., 2008). For each source type (pyrogenic, fossil and microbial), the diagonal elements of B per time step and lateral grid cell are proportional to the prior flux, or $f \times x_0$. Off-diagonal elements of B are constructed assuming an exponential decay of the prior error correlation in space and time with source-specific scales λ and τ respectively. The values of f, λ and τ for the different source types are given in Table 1. While there is no unique way of specifying these parameters, our choices yield reasonable 1σ prior uncertainties on global total microbial, fossil and pyrogenic emissions of $\sim 25\,\mathrm{Tg\,yr^{-1}}$ ($\sim 7\%$), $\sim 30\,\mathrm{Tg\,yr^{-1}}$ ($\sim 17\%$) and

Table 1. Parameters for constructing the prior flux error covariance

Source type	f	λ (km)	τ (months)
Microbial	1.2	500	2
Fossil	1.5	700	6
Pyrogenic	1.0	300	1

$\sim 2\,\mathrm{Tg\,yr^{-1}}$ ($\sim$6%) respectively. The 1σ uncertainty on the annual global total CH$_4$ emission comes to $\sim 40\,\mathrm{Tg\,yr^{-1}}$ ($\sim$7%) with these choices. The cost function J of eq (12) is minimized over 50 iterations by a conjugate gradient minimizer utilizing the Lanczos algorithm (Lanczos, 1950; Courtier et al., 1998).

In TM5 4DVAR, we calculate $J(x)$ of eq (12) with TM5 and $\partial J/\partial x$ with its adjoint. A traditional variational estimation would require us to run the forward and adjoint models multiple times over the entire period over which we want to estimate fluxes. However, these model runs require a significant amount of time, and iterations must be performed in succession. For example, at our $3° \times 2°$ resolution, TM5 simulates a decade in 8 hours. So to perform an inversion over two decades with 50 iterations (one iteration is one forward and one adjoint model run), it would take $8 \times 2 \times 2 \times 50 = 1600$ hours, or 67 days just for the model runs, not counting time spent in the computing queue. This is impractical given the need to do tests required of any new inversion system. Therefore, we split up our target period into several inversions that were run in parallel as shown in Figure 2(a). A single forward run from 1984 to 2017 produced initial C and $C\delta'_a$ fields for all inversions. This forward run was identical to scenario "C_WL+" of Lan et al. (2021) and matched the long term atmospheric CH$_4$ and δ^{13}CH$_4$ trends over that period. Six five-year inversions were run simultaneously with two years of overlap (red bars) between inversions, starting in 1997, 2000, 2003, 2006, 2009 and 2012. After all six inversions finished, the fluxes from the middle three-year period of each inversion (blue bars) were considered for analysis. For simulating prior and posterior mole fractions, fluxes from the non-overlapping periods (1997 – 2001, 2001 – 2004, 2004 – 2007 ... 2013 – 2017) were stitched together and a single forward run was done with those fluxes.

2.3 Prior fluxes and δ^{13}CH$_4$ source signatures

The prior fluxes and their δ^{13}CH$_4$ source signatures for the different categories of methane emissions are described in detail as "scenario C_WL+" in Lan et al. (2021). Briefly, the prior fluxes are based on bottom-up emission estimates with adjustments to match global atmospheric CH$_4$ increases and to satisfy the global mass balance of δ^{13}CH$_4$ over 1984–2017. For biomass burning or pyrogenic emissions, we use the Global Fire Emission Database (GFED) 4.1s for 1997-2016 (van der Werf et al., 2017) and estimates from the Reanalysis of Tropospheric chemical composition (RETRO) project before 1997 (Schultz et al., 2008). Other anthropogenic emissions are based on the EDGAR 4.3.2 inventory (Janssens-Maenhout et al., 2019). We use natural fossil emissions reported by Etiope et al. (2019). Emission estimates from wild animals and termites are adopted from Houweling et al. (1999) and Sanderson (1996) respectively. Wetland emissions and upland soil consumption of methane are
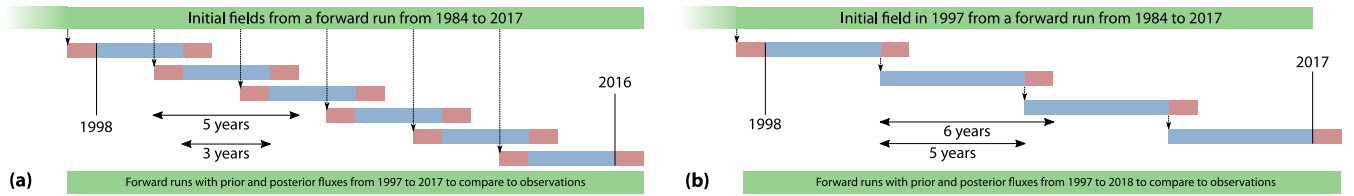
Figure 2. A schematic of the time splitting of our inversions. Red bars denote spin up and spin down periods, and blue bars denote periods from which fluxes were considered in our analysis. Schematic (a) denotes the time splitting used in most of our inversions as described in § 2.2, whereas schematic (b) denotes the time splitting used specifically with climatological priors as described in § 3.4. In splitting scheme (a), each inversion spans five years and the entire time span is covered with six inversions running simultaneously, starting from initial fields produced by a 1984–2017 model run with prior fluxes. In splitting scheme (b), each inversion spans six years and the entire span is covered with four inversions. However, except for the 1997–2003 inversion, all other inversions are started from the optimized mole fraction fields at the end of year 5 of the previous inversion, and therefore the inversions cannot be run in parallel.

estimated by a process-based model (Zhuang et al., 2004; Liu et al., 2020), after which the soil sink is modeled as a 1st order loss process as explained in § 2.4.

155   The $\delta^{13}CH_4$ source signatures used in our study are mainly spatially resolved maps based on the Global $\delta^{13}CH_4$ Source Signature Inventory 2020 for coal, oil and gas (ONG), biomass and biofuel burning, ruminant and wild animal sources (Sherwood et al., 2021; Lan et al., 2021), spatial maps for geological seeps (Etiope et al., 2019) and wetland sources (Ganesan et al., 2018). Globally averaged values are used for waste, landfills, termites, rice, and other energy and industry, given insufficient data to develop spatial distributions for their $\delta^{13}CH_4$ signatures (Lan et al., 2021).

160   The sum of the bottom-up methane emission estimates described above is not consistent with top-down estimates of global total emissions based on observed atmospheric CH_4 growth and estimated loss, which requires a $46\,Tg\,yr^{-1}$ increase in the annual global emission in 2016 compared to the 1999–2006 quasi-stable period. In addition, the $\delta^{13}CH_4$ mass balance requires $167\,Tg\,yr^{-1}$ emissions from fossil sources (including natural geological seeps) to be consistent with modeled sinks and the $\delta^{13}CH_4$ source signatures described above. Therefore, we (i) scale the ONG emissions from EDGAR 4.3.2 uniformly using

165   annual scaling factors to reach a total of $167\,Tg\,yr^{-1}$ from all fossil sources, (ii) impose a linear trend on wetland emissions to achieve an increase of $46\,Tg\,yr^{-1}$ in total 2016 emissions compared to 1999–2006, and (iii) adjusted emissions from agricultural and wastes sectors to match the year on year global CH_4 growth rate derived from marine boundary layer observations (Dlugokencky et al., 2011). This ensures that our global CH_4 and $^{13}CH_4$ budgets approximate the long term trends in atmospheric CH_4 and $\delta^{13}CH_4$ over 1984–2017.

170 **2.4   Methane loss mechanisms and fractionation**

Atmospheric methane has four loss mechanisms, atmospheric oxidation by OH and Cl throughout the atmosphere, destruction by $O(^1D)$ in the stratosphere, and surface uptake by upland soils. In all our inversions, these sinks are prescribed and not optimized. Monthly climatological CH_4 loss rates in the stratosphere due to OH, Cl and $O(^1D)$ were constructed from a run

Table 2. Fractionation parameters for CH$_4$ loss

Loss reaction	C	D (K)	Reference
Loss to OH	1.0039	0.00	Saueressig et al. (2001)
Loss to Cl	1.0430	6.46	Saueressig et al. (2001)
Loss to O(^{1}D)	1.0130	0.00	Saueressig et al. (2001)
Soil sink	1.0215	0.00	King et al. (1989)

of the ECHAM5/MESSy1 chemistry transport model (Steil et al., 2003; Jöckel et al., 2006). Loss due to tropospheric Cl is
175 simulated using a recent model-derived estimate of tropospheric Cl (Hossaini et al., 2016). For tropospheric OH, we use the
monthly OH climatology of Spivakovsky et al. (2000) after scaling by 0.9 to match the declining atmospheric abundance of
methyl chloroform in the early 2000s (Montzka et al., 2011).

In most CH$_4$ inversions, upland soil sinks are folded into the net wetland flux. However, the soil sink fractionates strongly
between ^{12}CH$_4$ and ^{13}CH$_4$ (King et al., 1989), and therefore we keep it separate from wetland fluxes. We model the soil sink
180 as a first order reaction at the surface, in which the loss rates of ^{12}CH$_4$ and ^{13}CH$_4$ in the lowest model layer are $d^{12}C/dt =
-k_{ss}F_{ss}\,^{12}C$ and $d^{13}C/dt = -\alpha_{ss}k_{ss}F_{ss}\,^{13}C$ respectively. F_{ss} is the prior soil sink map from the TEM land surface model, and
k_{ss} is an arbitrary constant tuned to a value such that in a forward run with prior fluxes, the global total soil sink matches the
prior total.

The fractionation between ^{12}C and ^{13}C for each of the loss reactions is modeled as $k_{12}/k_{13} = 1/\alpha = Ce^{D/T}$ (Saueressig
185 et al., 2001), where T is the air temperature in Kelvin. The soil sink fractionation is cast in a similar form for convenience.
Coefficients C and D we used are tabulated in Table 2.

2.5 CH$_4$ and δ^{13}CH$_4$ measurements

To maximize the spatiotemporal coverage of in-situ CH$_4$ and δ^{13}CH$_4$ data, we have developed a new database by harmonizing
measurements from NOAA/INSTAAR with those from 30 other laboratories around the world (Lan et al., 2021). All CH$_4$ data
190 have been quality checked and converted to a common CH$_4$ scale, namely the World Meteorological Organization (WMO)
X2004A scale maintained at NOAA's Global Monitoring Laboratory (Dlugokencky et al., 2005). For data not on the WMO
X2004A scale, we applied lab-specific scale multipliers estimated based on (i) comparisons of measurements of common
air samples during the WMO/IAEA Round Robin Comparison Experiment (Crotwell et al., 2020), and (ii) comparisons of
co-located atmospheric measurements made by NOAA and other laboratories. We constructed the uncertainty on the assimi-
195 lated CH$_4$ measurements from a combination of (i) measurement repeatability of a single sample (hereafter called the single
measurement precision), (ii) lab-specific long-term reproducibility based on analyzer type and sampling frequency reported in
literature, and (iii) each lab's realization of the calibration scale. If a scale conversion was needed to bring measurements onto
the WMO X2004A scale, the mole fraction uncertainty due to the scale multiplier uncertainty was added in quadrature. The
final uncertainties are typically less than 9 ppb for all CH$_4$ measurements.

We used $\delta^{13}CH_4$ data from the Institute for Arctic and Alpine Research (INSTAAR) as well as other isotope laboratories making precise measurements of atmospheric methane with isotope ratio mass spectrometers. The INSTAAR $\delta^{13}CH_4$ data were measured in a subset of air samples collected from NOAA's Global Greenhouse Gas Reference Network (GGGRN). Because different labs have independent ties to primary reference materials which do not agree, we calculated offsets to bring the $\delta^{13}CH_4$ data onto the INSTAAR realization of the Vienna Pee Dee Belemnite (VPDB) scale (Miller et al., 2002). These offsets were based on measurements of cylinders, flasks filled from cylinders, or co-located sample data, and are all described in Umezawa et al. (2018). When there was not a direct comparison, e.g., between INSTAAR and TU, or INSTAAR and NIPR, we used comparisons between each of these labs and the Institute for Marine and Atmospheric research Utrecht (IMAU). Each comparison had an uncertainty associated with it, which were combined in quadrature to account for uncertainty in the offset correction. The total uncertainty on assimilated $\delta^{13}CH_4$ measurements was typically less than $0.15\,‰$. The final database of assimilated CH_4 and $\delta^{13}CH_4$ measurements is available at https://doi.org/10.15138/64w0-0g71.

With the following exceptions, we assimilate all the observations from this database including marine boundary layer sites, surface and tower sites over continents (Andrews et al., 2014), and vertical profiles from routine aircraft measurements (Sweeney et al., 2015). Intermittent aircraft profiles such as from the HIPPO (Wofsy, 2011) and ATom (Thompson et al., 2022) campaigns are not assimilated. CH_4 data from flasks taken aboard routine flights between Japan and Australia as part of the CONTRAIL program have been assimilated (Machida et al., 2008; Matsueda et al., 2015). A subset of the CONTRAIL flasks were also analyzed for $\delta^{13}CH_4$ (Umezawa et al., 2012), which were not assimilated. For continental tower sites with multiple intake heights, only data from the highest intake are considered in inversions to minimize local influence. For sites with continuous CH_4 analyzers, the CH_4 data are averaged hourly and only hourly averages between 11:00 and 16:00 local solar time are assimilated; these are the times when planetary boundary layer heights are likely to be best-represented by transport models. For continuous CH_4 analyzers on mountain tops, we only assimilate hourly averages between 00:00 to 05:00 local solar time to avoid possible up-slope contamination. Site-specific statistical filtering based on a non-parametric curve fitting routine (Thoning et al., 1989) is further applied, with the exception of vertical profiles, to remove large outliers with potential local or other contamination. The number of CH_4 and $\delta^{13}CH_4$ measurements assimilated each year is summarized in Table 3, and their locations are plotted in Figure 3.

2.6 Uncertainty estimation and sensitivity tests

The uncertainty of surface emission estimates is a combination of random and systematic uncertainties. Random uncertainties are associated with those components of the inversion system whose ~~variations~~ errors are assumed to be zero on average. In the formulation of the cost function (12), the prior flux x_0 is assumed to have a probability density function (PDF) centered on the true flux with variance around the truth given by the prior covariance matrix B. Similarly, the model-observation mismatch $Hx - y$ is assumed to have a PDF centered around the mismatch between the true atmospheric mole fraction and true fluxes propagated through an unbiased transport model, with variance around this mean given by R. The random uncertainty in the

Table 3. The number of CH$_4$ and δ^{13}CH$_4$ observations assimilated in our inversions, broken down by year.

Year	CH$_4$	δ^{13}CH$_4$	Year	CH$_4$	δ^{13}CH$_4$	Year	CH$_4$	δ^{13}CH$_4$
1997	9075	0	2004	24669	1178	2011	66307	1914
1998	9236	457	2005	36077	742	2012	74957	1842
1999	9981	371	2006	36707	1163	2013	70785	1592
2000	33514	537	2007	44056	1042	2014	81433	2171
2001	16514	256	2008	51138	990	2015	84900	2576
2002	19497	925	2009	53243	1875	2016	81126	2941
2003	20191	1070	2010	66930	1413	2017	57977	2337
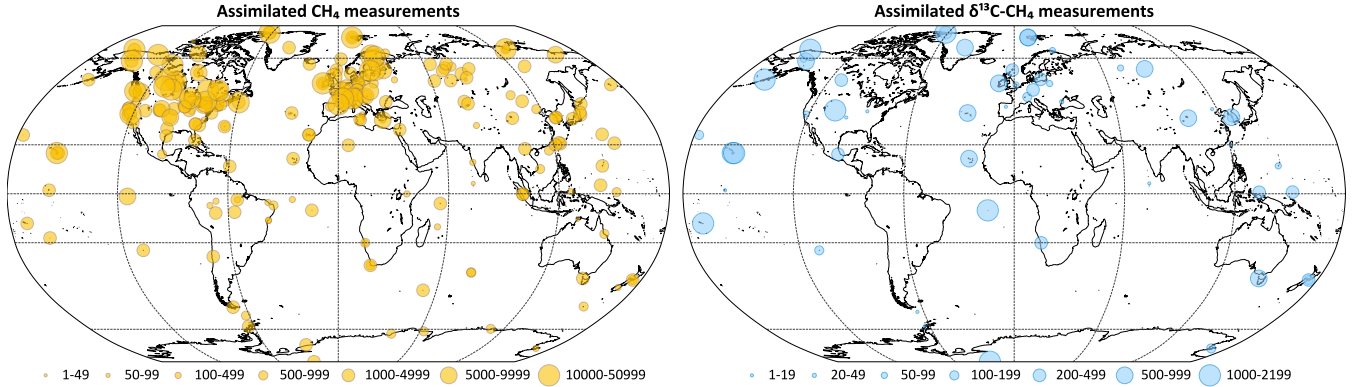
Figure 3. Locations of assimilated CH$_4$ and δ^{13}CH$_4$ measurements. The symbol sizes represent the number of measurements between 1997–2017 assimilated from each location. Overlapping symbols over some of the locations are due to multiple agencies measuring at those locations.

optimal estimate is given by $\hat{B}$, where

$$\hat{B}^{-1} = \frac{\partial^2 J}{\partial x^2} = H^T R^{-1} H + B^{-1} \tag{13}$$

Variational inversion systems such as TM5 4DVAR can construct a low rank approximation of $\hat{B}$ during the optimization. However, for large state vectors the $\hat{B}$ thus constructed is an overestimation of the true posterior uncertainty (Meirink et al., 2008; Bousserez et al., 2015). We therefore construct an estimate of $\hat{B}$ by performing an ensemble of 100 independent inversions for each of the 5-year inversions of Figure 2(a), with prior fluxes and observations perturbed according to the covariances specified by B and R respectively. With 100 ensemble members, our estimate of $\hat{B}$ is expected to be within $10\,\%$ of the exact analytical solution for $\hat{B}$ (Bousserez et al., 2015). Furthermore, our ensemble of inversions allows us to compute any posterior covariance and correlation between estimated fluxes, such as between large regions or different CH$_4$ source types.

Systematic uncertainties are associated with aspects of the inversion system that are assumed fixed and perfectly known in principle, but might in fact be biased in practice. In our inversion system, such aspects include, but are not limited to, atmospheric transport and chemistry, isotope source signatures, and the wetland inundation maps used to construct the prior wetland emissions. Because the posterior covariance estimate does not include systematic errors, we explore the impact of such errors by performing inversions with different realizations of those potentially biased inputs in the following sensitivity tests.

2.6.1 Tropospheric chlorine

The magnitude and distribution of the Cl sink in the troposphere is uncertain, with estimates as high as $13\,\mathrm{Tg\,yr^{-1}}$ to $37\,\mathrm{Tg\,yr^{-1}}$ based primarily on southern hemisphere background observations (Allan et al., 2007). However, more recent studies have found a more limited role of tropospheric Cl as a methane oxidant (Gromov et al., 2018). Consequently, most CH_4 inverse models neglect tropospheric Cl as a methane oxidant. However, due to the strong isotopic fractionation in the $CH_4 + Cl$ reaction, Cl plays an important role in determining atmospheric $\delta^{13}CH_4$ (Strode et al., 2020; Lan et al., 2021). It is therefore important to test the sensitivity of our conclusions to the imposed tropospheric Cl sink within the range of realism. The Cl estimate by Hossaini et al. (2016) we use in this study is on the higher side of the range posited by Gromov et al. (2018). We perform an inversion with the tropospheric Cl field reported by Wang et al. (2021) as an alternative lower specification. In order to keep the global CH_4 lifetime unchanged between the two scenarios of tropospheric Cl, we scale the tropospheric OH field by 0.9 and 0.92 respectively when we use the Cl fields of Hossaini et al. (2016) and Wang et al. (2021). Since the two scenarios lead to slightly different sink fractionation in the atmosphere, prior ONG and ruminant fluxes are adjusted to match the long term atmospheric $\delta^{13}CH_4$ trend for both cases.

2.6.2 OH fractionation

We use chemical fractionation factors reported by Saueressig et al. (2001) since they provide factors for all atmospheric sink processes from a consistent set of laboratory measurements. While these are the most recent and generally accepted, for CH_4 oxidation by OH another set of coefficients $C = 1.0054, D = 0$ have previously been reported by Cantrell et al. (1990). To the best of our knowledge, this earlier result has not been refuted in the literature, nor is there any independent evidence supporting one set of coefficients over another. Instead, the most recent evaluation of atmospheric reaction rates (Burkholder et al., 2019) recommends using the Saueressig et al. (2001) rates with increased uncertainty in the OH fractionation to include Cantrell et al. (1990) as a possibility. Since the sink fractionation plays a significant role in determining atmospheric $\delta^{13}CH_4$, we perform an additional inversion with the OH fractionation of Cantrell et al. (1990) to gauge its impact. Since the two OH fractionation factors lead to different sink fractionation in the atmosphere, prior ONG and ruminant fluxes are adjusted to match the long term atmospheric $\delta^{13}CH_4$ trend for both cases.

2.6.3 $\delta^{13}CH_4$ source signatures

In principle, it is possible to estimate both CH_4 fluxes and $\delta^{13}CH_4$ source signatures in a dual tracer inversion (Thanwerdas et al., 2021). However, this makes the problem non-linear and the inversion convergence slow. It is also difficult to construct a prior covariance for $\delta^{13}CH_4$ source signatures since much of the uncertainty stems from extrapolating a limited number of $\delta^{13}CH_4$ signature measurements to the entire domain of CH_4 sources, resulting in errors that are systematic and non-Gaussian. Therefore, we explore the impact of $\delta^{13}CH_4$ signature uncertainty on our results by running inversions with alternate specifications of $\delta^{13}CH_4$ signature maps as follows.

Source signature maps for biomass burning were calculated by multiplying C3 and C4 signatures of $-26.7\%_o$ and $-12.5\%_o$ respectively (Cerling et al., 1998) with the C3/C4 fraction for each $1° \times 1°$ latitude/longitude grid cell (Lan et al., 2021). For ruminants and wild animals, C3 and C4 signatures were taken to be $-54.5\%_o$ and $-67.8\%_o$ respectively from the Global $\delta^{13}CH_4$ Source Signature Inventory 2020 (Sherwood et al., 2021; Lan et al., 2021). In this way, the C3/C4 vegetation distribution determines the source signatures of both biomass burning and ruminant emissions. Our default inversion averages the C3/C4 distributions of Still et al. (2003) and its modified version as used by Randerson et al. (2012). To explore the uncertainty from the assumed C3/C4 map, we perform two additional inversions with $\delta^{13}CH_4$ source signature maps derived separately from the two individual C3/C4 distributions. In addition, country-level ruminant emission signatures were compiled by Chang et al. (2019), including their temporal changes due to shifting ruminant diet and due to the downward trend in atmospheric $\delta^{13}CO_2$ that is photosynthesized by the vegetation. We use the ruminant CH_4 source signatures of Chang et al. (2019) in a third inversion. The three instances of source signatures related to the C3/C4 distribution described here were significantly different, requiring us to adjust the prior flux apportionment to meet our goal of matching long-term CH_4 and $\delta^{13}CH_4$ trends. Specifically, we changed the prior fossil CH_4 emissions from the default of $167\,\mathrm{Tg\,yr^{-1}}$ to $158\,\mathrm{Tg\,yr^{-1}}$ for the inversions using $\delta^{13}CH_4$ signatures derived from Still et al. (2003) and Chang et al. (2019). For the inversion using $\delta^{13}CH_4$ signatures derived from Randerson et al. (2012), we adjusted the prior fossil emission to $175\,\mathrm{Tg\,yr^{-1}}$. In all cases, this was achieved by globally scaling the ONG and ruminant emissions to achieve long-term CH_4 and $^{13}CH_4$ mass balance.

For the global maps of ONG and coal emission signatures, our default inversion assumes time-invariant maps over the study period. However, considering the rapid development of the US shale gas production and a shift in production from conventional to shale gas in the past decades, we estimate that the mean US ONG signature (production-weighted mean of shale and conventional gas) increased by $2.7\%_o$ from 2006 to 2016 (Lan et al., 2021). We incorporate this in an alternate specification of fossil CH_4 source signatures and perform an inversion with this new map.

Finally, our default inversion setup uses the latitude-based source signature specification of Ganesan et al. (2018) for wetland emissions. Over the past several years we have implemented carbon isotopes in the TEM land surface model (Zhuang et al., 2004), making it possible to derive process-based $\delta^{13}CH_4$ wetland source signatures consistent with wetland emissions (IsoTEM, Oh et al., 2022). We perform an inversion with wetland source signatures from the IsoTEM model as an alternative to our default wetland source signatures.

2.6.4 Wetland inundation extent

Wetland inundation extent is a leading driver of uncertainty in bottom-up estimates of wetland CH_4 emissions, and therefore in
the global CH_4 budget. We explore this uncertainty by performing inversions with prior wetland CH_4 fluxes derived from the
TEM model (Zhuang et al., 2004) driven by two different inundation maps. Our default setup uses a time-varying or dynamic
inundation map based on the satellite-based Surface WAter Microwave Product Series (SWAMPS, Schroeder et al., 2015)
combined with the Global Lakes and Wetlands Dataset (GLWD, Lehner and Döll, 2004; Poulter et al., 2017). In addition, we
also drive the TEM model with the static inundation map of Matthews and Fung (1987), in which case meteorology is the only
source of seasonal and inter-annual variation of prior wetland emissions. These two inundation maps produce significantly
different atmospheric CH_4 and $\delta^{13}CH_4$ gradients (scenarios "C_WL+" and "Q_static_WL" of Lan et al., 2021) in a forward
run, and therefore serve as a robust test of our inversion results with different inundation extents.

2.6.5 Initial $\delta^{13}CH_4$ gradients

Large scale gradients of atmospheric $\delta^{13}CH_4$ take significantly longer to respond to changes in emissions compared to gradients
of CH_4 (Tans, 1997), requiring multi-decade spin-ups for models trying to simulate atmospheric $\delta^{13}CH_4$ (Lan et al., 2021).
Inverse models, on the other hand, take significantly less time to be spun-up since fluxes during the spin-up period are modified
to fit observed atmospheric $\delta^{13}CH_4$. The exact spin-up duration required depends on the accuracy of the initial modeled $\delta^{13}CH_4$
gradients and the inversion setup. To test if a one year spin-up for our inversions as depicted in Figure 2(a) is sufficient,
we perform two additional inversions with different starting $\delta^{13}CH_4$ large-scale gradients. Specifically, of the flux scenarios
simulated by Lan et al. (2021), we choose scenarios "H_mean_sig" and "Q_static_WL", which produced the flattest and
steepest north-south gradients in $\delta^{13}CH_4$ respectively (see Lan et al., 2021, Figure 5). We perform inversions starting from
CH_4 and $\delta^{13}CH_4$ fields provided by forward simulations of those scenarios at each of the starting points in Figure 2(a). The
resultant spread in fluxes provides an estimate of the sensitivity of our setup to erroneous initial $\delta^{13}CH_4$ gradients.

3 Results

3.1 Fit to atmospheric CH_4 and $CH_4 + \delta^{13}CH_4$ data

Both the CH_4-only and the $CH_4 + \delta^{13}CH_4$ inversions fit the atmospheric CH_4 data, while only the latter is consistent with
atmospheric $\delta^{13}CH_4$ data. This is demonstrated both at surface sites from which data were assimilated, as well as data from
aircraft campaigns that were withheld for validation. Figure 4 shows that both inversions fit the observed CH_4 time series at
three NOAA baseline observatories. However, despite starting from realistic atmospheric CH_4 and $\delta^{13}CH_4$ fields, the CH_4-only
inversion moves progressively farther from observed $\delta^{13}CH_4$ with time at those same locations, demonstrated in Figure 5. Only
the $CH_4 + \delta^{13}CH_4$ inversion fits both atmospheric CH_4 and $\delta^{13}CH_4$ data. This is also demonstrated in Figure 6, which compares
modeled $\delta^{13}CH_4$ to $\delta^{13}CH_4$ measured by the HIPPO and ATom aircraft campaigns, and from regular flights between Japan and
Oceania as part of the CONTRAIL program. ATom and HIPPO campaigns sampled primarily background air over the oceans
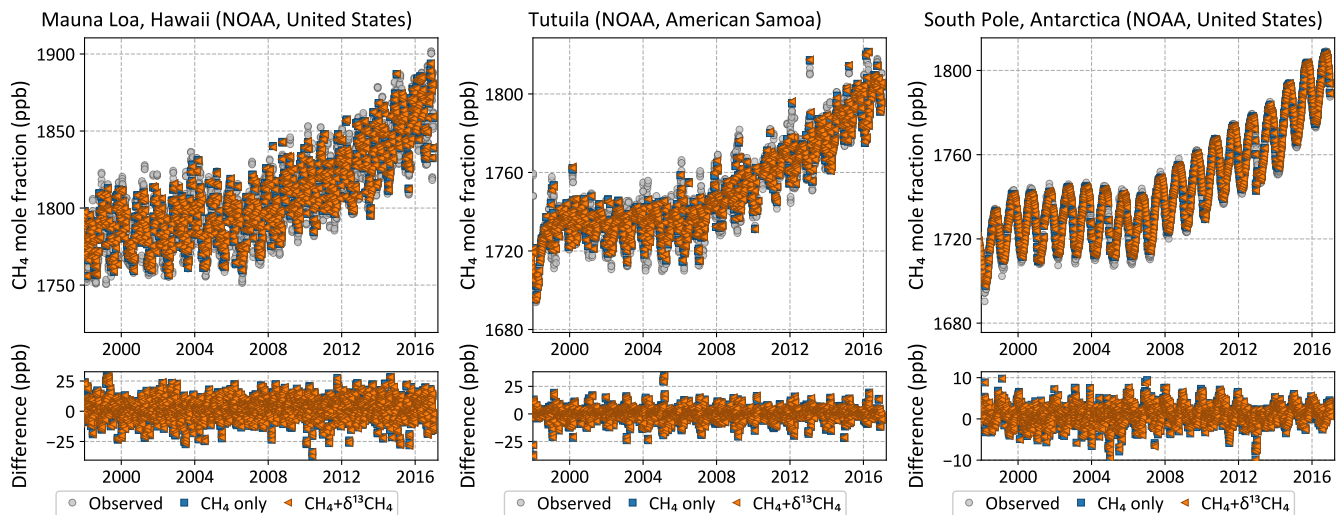
Figure 4. Observed (grey circles) and posterior modeled (colored symbols) CH$_4$ time series at three NOAA baseline observatories. Both inversions with and without δ^{13}CH$_4$ data fit the CH$_4$ data equally well.
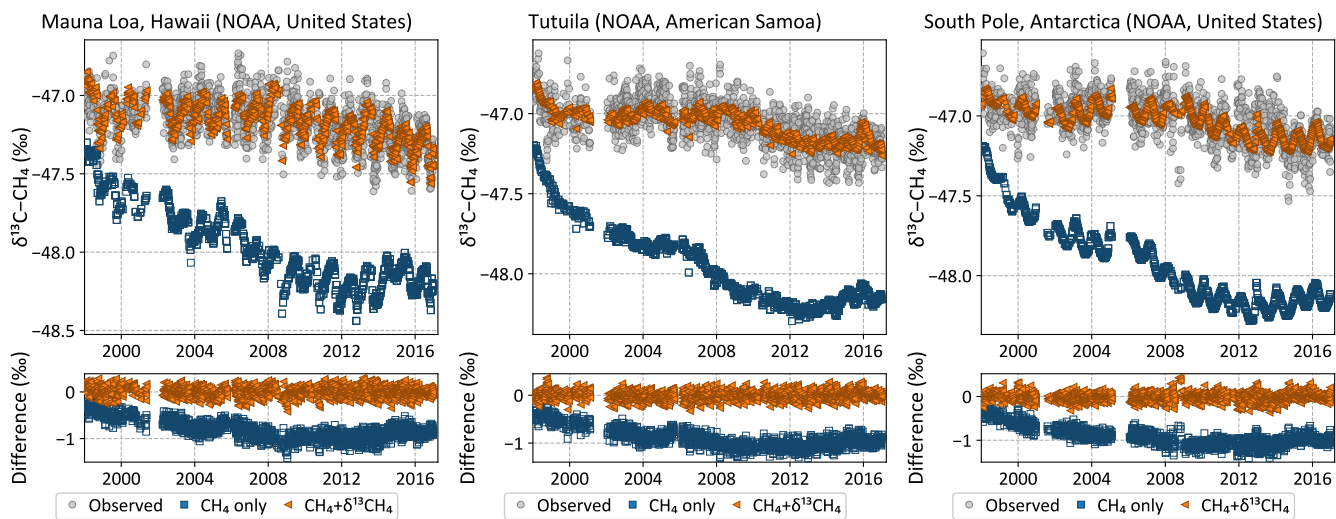
Figure 5. Observed (grey circles) and posterior modeled (colored symbols) δ^{13}CH$_4$ time series at three NOAA baseline observatories. The inversion with δ^{13}CH$_4$ data fit the observations throughout the inversion period, but the inversion without δ^{13}CH$_4$ data – a traditional CH$_4$ inversion – drifts away from the observations with time. Note that both inversions were started with the same CH$_4$ and δ^{13}CH$_4$ fields in 1997, but by the time δ^{13}CH$_4$ data were available in mid-1998 they had already drifted apart, leading to the apparent initial offset in the plots above.
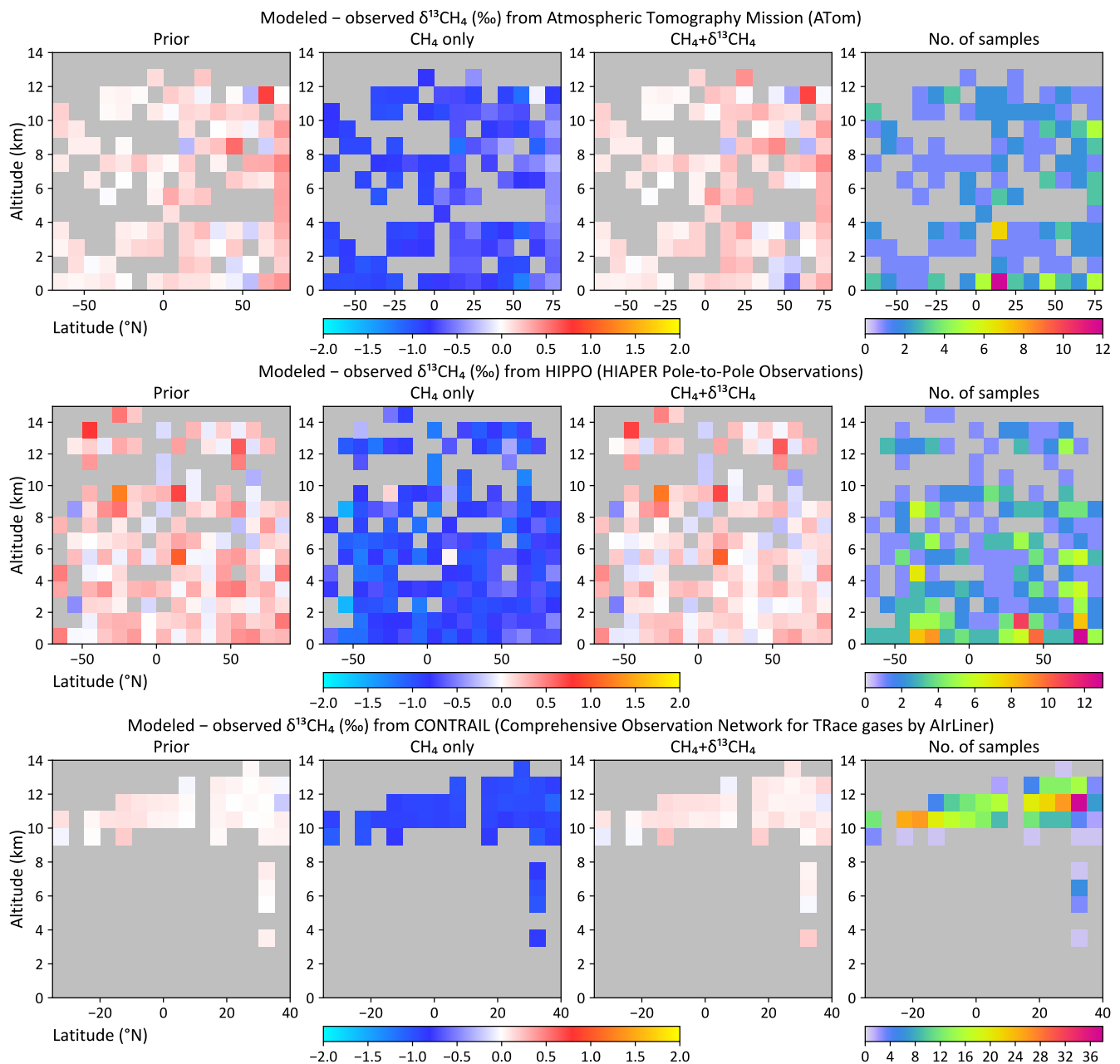
Figure 6. Modeled minus observed $\delta^{13}CH_4$ as a function of latitude and altitude from the ATom (top), HIPPO (middle) and CONTRAIL (bottom) aircraft campaigns. Mismatches are shown for the prior flux, the CH_4-only inversion, and the dual tracer $CH_4 + \delta^{13}CH_4$ inversion. Altitudes have been binned in 1 km bins, while latitudes have been binned either in 10° (ATom, HIPPO) or 5° (CONTRAIL) bins. The rightmost panels show the number of samples averaged per bin.

at multiple latitudes and altitudes, and neither CH_4 nor $\delta^{13}CH_4$ data from those campaigns were assimilated. CONTRAIL primarily sampled the marine background at multiple altitudes as well, except for a small number of samples taken during takeoff and touchdown in Japan. CH_4 flask samples from CONTRAIL were assimilated in both inversions, but their $\delta^{13}CH_4$ measurements were not assimilated. The CH_4-only inversion compares far less favorably to the $\delta^{13}CH_4$ measurements than the joint inversion. Therefore, it is reasonable to conclude that our CH_4-only inversion, and very likely most traditional CH_4-only inversions, do not yield a CH_4 emission distribution consistent with atmospheric $\delta^{13}CH_4$ observations. We therefore expect our $CH_4 + \delta^{13}CH_4$ inversion to provide more accurate emission estimates and source partitioning than our CH_4-only inversion.

3.2 Large scale fluxes from CH_4 and $CH_4 + \delta^{13}CH_4$ inversions

~~Total and source-specific annual emissions of CH_4 globally and from three latitudinal bands. "Tropics" in this context refers to the region between and , while the northern and southern extra-tropics are to the north and south respectively. The shaded regions denote 2σ prior and posterior error bars.~~

~~Annual averages of CH_4 emissions between 1999–2016 and their 2σ uncertainties shown in Figure 7, in . The "CH_4 only" and "CH_4+" inversions of Figure 7 have been abbreviated to "CH_4" and "Joint" respectively below. Note that (a) the 2σ uncertainties tabulated are the averages of the uncertainties across 18 years, *not* the uncertainties on the 18 year average emissions, and (b) an uncertainty of zero below is due to rounding, and not because the uncertainty is exactly zero. Source type(r)1-1(lr)2-4(lr)5-7(lr)8-10(lr)11-13InversionPriorCH4JointPriorCH4JointPriorCH4JointPriorCH4JointGlobe 57779 5764 5764 38352 40713 37413 16759 14113 17313 283 283 303 Northern Extra-Tropics 31868 27310 27410 18839 16414 16814 12055 9913 9613 102 102 102 Tropics 22131 27111 26911 16327 21613 18413 4115 3810 6610 173 162 192 Southern Extra-Tropics 3812 324 324 3211 275 225 64 43 103 10 10 10~~

The top row of Figure 7 shows the global total annual emissions from two inversions, a CH_4-only or "traditional" methane inversion without $\delta^{13}CH_4$ data, and a joint $CH_4 + \delta^{13}CH_4$ inversion developed in this work. The shaded regions in Figure 7 denote 2σ random errors derived from 100-member Monte Carlo ensembles of inversions described in § 2.6. Annual averages of the emissions and random errors are summarized in Table 4. Since many methane studies calculate emissions between and outside of the $\pm 30°$ latitude band, in Table 4 we report those numbers as well for ease of comparison. The global total emission from all categories is unaffected by the addition of $\delta^{13}CH_4$ data, since $\delta^{13}CH_4$ does not place any additional constraint on the total CH_4 emission. However, the partitioning between microbial and fossil sources is changed significantly with the addition of $\delta^{13}CH_4$ data. Based on comparison to atmospheric data as noted in § 3.1, we expect the source partitioning from our $CH_4 + \delta^{13}CH_4$ inversion to be more accurate compared to our traditional CH_4-only inversion.

Figure 7 also shows the total and source-disaggregated CH_4 emissions from our CH_4 and $CH_4 + \delta^{13}CH_4$ inversions over three latitude bands, where the Tropics are bounded between 23.5 °S and 23.5 °N. Relative to the prior, tropical (extra-tropical) total emissions are adjusted upward (downward) by both inversions, and there is little sensitivity of the tropical versus extra-tropical partitioning on the assimilation of $\delta^{13}CH_4$ data. In the northern extra-tropics, the partitioning of CH_4 emissions between the different source types does not change significantly with the addition of $\delta^{13}CH_4$ data. However, in the Tropics the inversion with $\delta^{13}CH_4$ data shows significantly higher fossil (and lower microbial) emissions than the inversion without $\delta^{13}CH_4$ data.

Fossil CH$_4$ emissions in the southern extra-tropics are significantly different for most years in the presence of δ^{13}CH$_4$ data, but similarly significant differences do not exist for the other source types. Finally, our estimate of pyrogenic emissions does not change significantly in Figure 7 in the presence and absence of δ^{13}CH$_4$.
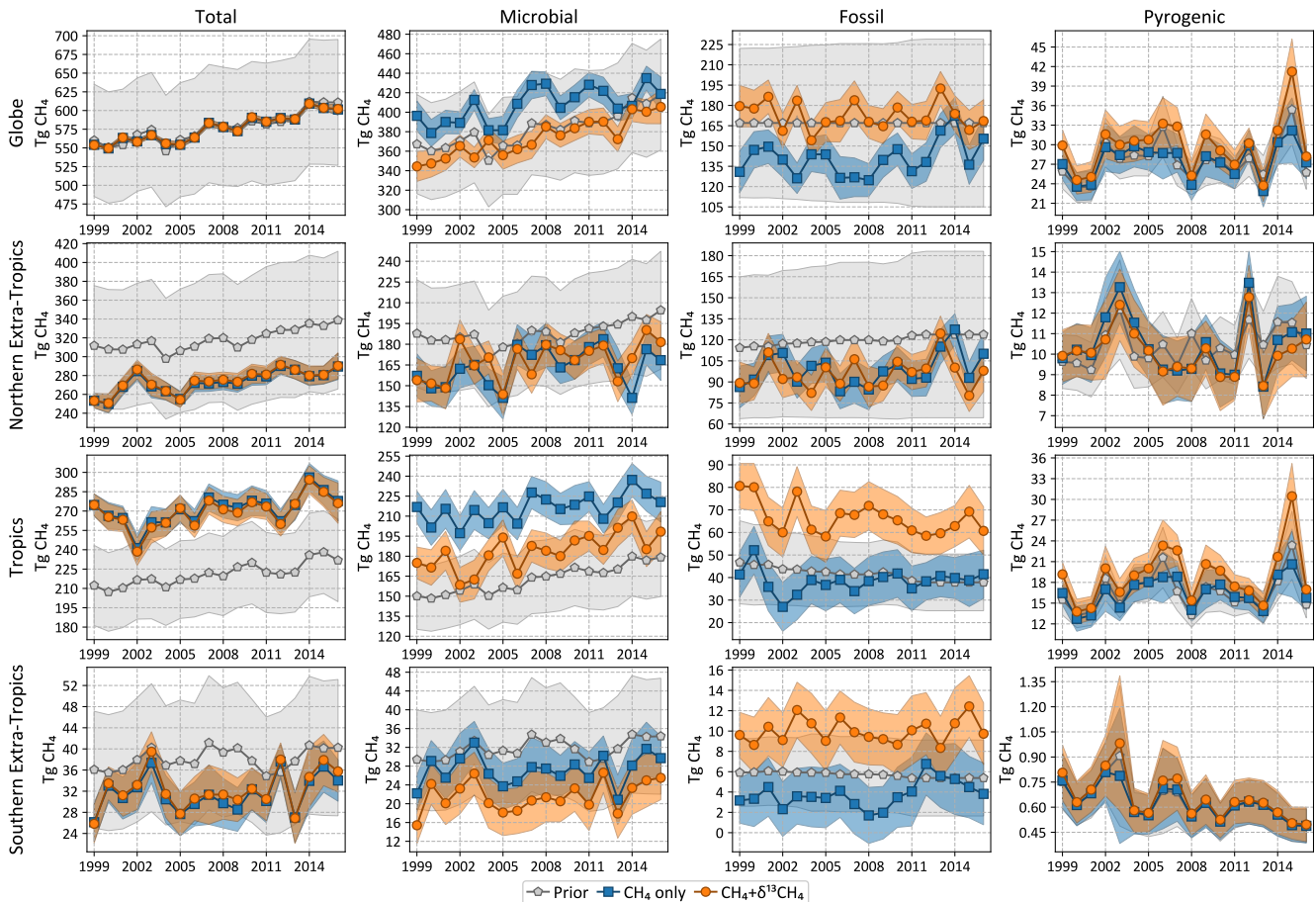
Figure 7. Total and source-specific annual emissions of CH$_4$ globally and from three latitudinal bands. "Tropics" in this context refers to the region between 23.5 °N and 23.5 °S, while the northern and southern extra-tropics are to the north and south respectively. The shaded regions denote 2σ prior and posterior error bars.

3.3 Systematic errors in emission estimates

As explained in § 2.6, we estimate possible biases in our flux estimates by running the inversion with different choices of non-optimized input. The spread in annual emissions due to alternate specifications of atmospheric chemistry (tropospheric chlorine of § 2.6.1 and OH fractionation of § 2.6.2) is shown in Figure 8. Analogous spreads due to different specifications of δ^{13}CH$_4$ source signatures (§ 2.6.3), wetland inundation maps (§ 2.6.4) and initial atmospheric δ^{13}CH$_4$ fields (§ 2.6.5) are

Table 4. Annual averages of CH_4 emissions between 1999–2016 and their 2σ uncertainties shown in Figure 7 and three additional zonal bands, in $Tg\,yr^{-1}$. The "CH_4 only" and "$CH_4 + \delta^{13}CH_4$" inversions of Figure 7 have been abbreviated to "CH_4" and "Joint" respectively. Note that (a) the 2σ uncertainties tabulated are the averages of the uncertainties across 18 years, *not* the uncertainties on the 18 year average emissions, and (b) zeroes below are due to rounding to the nearest integers, not because the concerned quantities are exactly zero.

Source type	Total			Microbial			Fossil			Pyrogenic		
Inversion	Prior	CH_4	Joint	Prior	CH_4	Joint	Prior	CH_4	Joint	Prior	CH_4	Joint
Globe	577 ± 79	576 ± 4	576 ± 4	383 ± 52	407 ± 25	374 ± 13	167 ± 59	141 ± 25	173 ± 13	28 ± 3	28 ± 3	30 ± 3
Northern Extra-Tropics	318 ± 68	273 ± 10	274 ± 10	188 ± 39	164 ± 21	168 ± 14	120 ± 55	99 ± 22	96 ± 13	10 ± 2	10 ± 2	10 ± 2
Tropics	221 ± 31	271 ± 10	269 ± 11	163 ± 27	216 ± 14	184 ± 13	41 ± 15	38 ± 11	66 ± 10	17 ± 3	16 ± 2	19 ± 2
Southern Extra-Tropics	38 ± 12	32 ± 4	32 ± 4	32 ± 11	27 ± 5	22 ± 5	6 ± 4	4 ± 3	10 ± 3	1 ± 0	1 ± 0	1 ± 0
North of 30 °N	254 ± 59	247 ± 9	247 ± 9	145 ± 31	138 ± 19	147 ± 13	101 ± 50	101 ± 20	92 ± 13	8 ± 1	8 ± 1	8 ± 1
30 °S–30 °N	302 ± 43	319 ± 10	319 ± 11	219 ± 37	259 ± 16	221 ± 14	63 ± 22	40 ± 15	76 ± 13	20 ± 3	19 ± 2	22 ± 2
South of 30 °S	21 ± 8	10 ± 4	11 ± 4	18 ± 7	10 ± 4	6 ± 4	3 ± 2	0 ± 2	4 ± 2	0 ± 0	0 ± 0	0 ± 0

shown in Figure 9. Note that the Y-axis ranges in Figures 8 and 9 are different. The average spread in annual emissions from different latitude bands and source types are summarized in Table 5 for each sensitivity test. The average of the annual posterior uncertainties as depicted in Figure 7 are also provided in Table 5 as "MC-derived (2σ)" for reference, with the caveat that 2σ uncertainties are not directly comparable to the range across a few inversions.

380 Most of the sensitivity tests have little impact on the global total CH_4 emission, and the spread in the total CH_4 emission from different latitude bands is generally smaller than the posterior uncertainty of our base inversion. However, by far the largest source of error in partitioning the total emission into fossil and microbial sources comes from our representation of atmospheric chemistry, namely the distribution of tropospheric chlorine and the kinetic isotope effect of CH_4 destruction by OH. Unless the uncertainty in these two factors can be reduced, our ability to use $\delta^{13}CH_4$ measurements to partition different

385 source types will be seriously hampered. The uncertainty arising from our limited knowledge of $\delta^{13}CH_4$ source signatures, to the extent represented by the different signature maps used, is lower than the uncertainty due to atmospheric chemistry. Lastly, the uncertainty due to an incorrect specification of the initial atmospheric $\delta^{13}CH_4$ field is minimal, in line with our expectation that an inversion will rapidly correct for it by adjusting emissions during its spin-up period. However, we note here that the "incorrect" initial fields we constructed for the last test still satisfied the global $\delta^{13}CH_4$ mass balance by construction. The

390 sensitivity to an incorrect initial condition will likely be higher if the initial field does not satisfy global $\delta^{13}CH_4$ mass balance.

3.4 Attribution of the post-2007 methane growth

As discussed earlier (Figure 1 and discussion in § 1), the atmospheric methane burden has been steadily growing since 2007 after a period of quasi-stability during 1999–2006. We use our $CH_4 + \delta^{13}CH_4$ inversion to ask whether the addition of $\delta^{13}CH_4$ data can provide information on the sources of the additional methane. Figure 7 suggests that the trend in CH_4 emissions comes largely from microbial emissions in a $CH_4 + \delta^{13}CH_4$ inversion. However, it is possible that this attribution to microbial
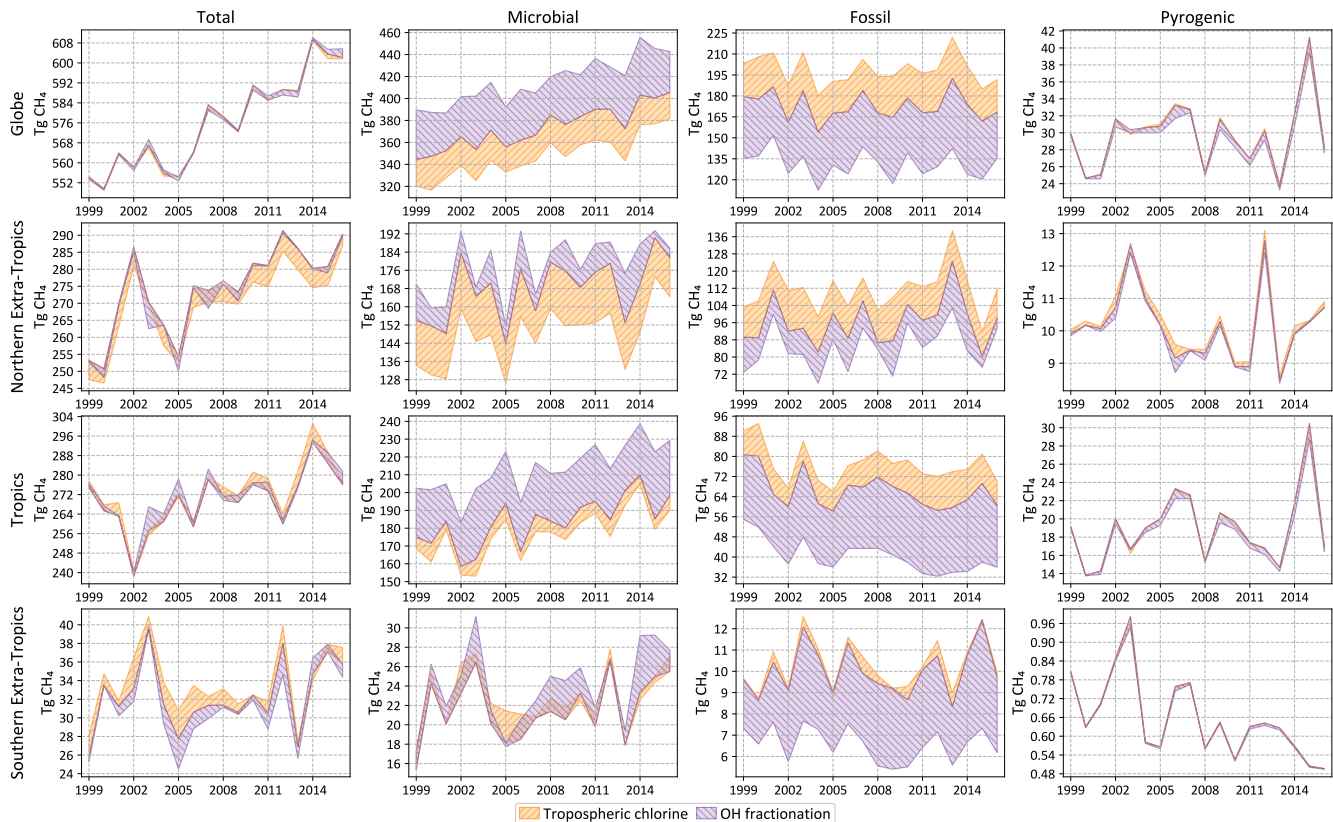
Figure 8. Total and source-specific annual emissions of CH$_4$ globally and from three latitudinal bands as in Figure 7. The shaded regions denote the spread (max to min) of annual emissions from sensitivity tests described in § 2.6.1 and § 2.6.2. A stronger OH fractionation makes the atmosphere heavier, requiring a larger (smaller) fraction of microbial (fossil) to match the same observations. A smaller chlorine sink makes the atmosphere lighter, requiring a smaller (larger) fraction of microbial (fossil) to match the same observations. That is, a stronger OH fractionation and a smaller chlorine sink affect the fossil/microbial partitioning in opposite ways, resulting in the structure seen here.

emissions comes from our prior – which had a trend in the microbial emissions and a temporally flat fossil contribution – instead of the atmospheric data. To assess the robustness of our inferred microbial and fossil emission trends, we perform a second set of inversions with the following modifications:

1. We construct climatological prior fluxes and source signatures by averaging our prior emissions and signatures from 2000 to 2006. Neither the resulting priors nor the source signatures have any time trend.

2. Since the methane budget from climatological priors is no longer in balance with the atmospheric growth, we cannot use the overlapping inversions of Figure 2(a) to run multiple periods in parallel. Instead, we run four 6-year inversions in sequence, spanning 1997–2003, 2002–2008, 2007–2013 and 2012–2018, following the scheme shown in Figure 2(b). The first inversion used the same initial field in 1997 as our default inversion. Every successive inversion used the

400
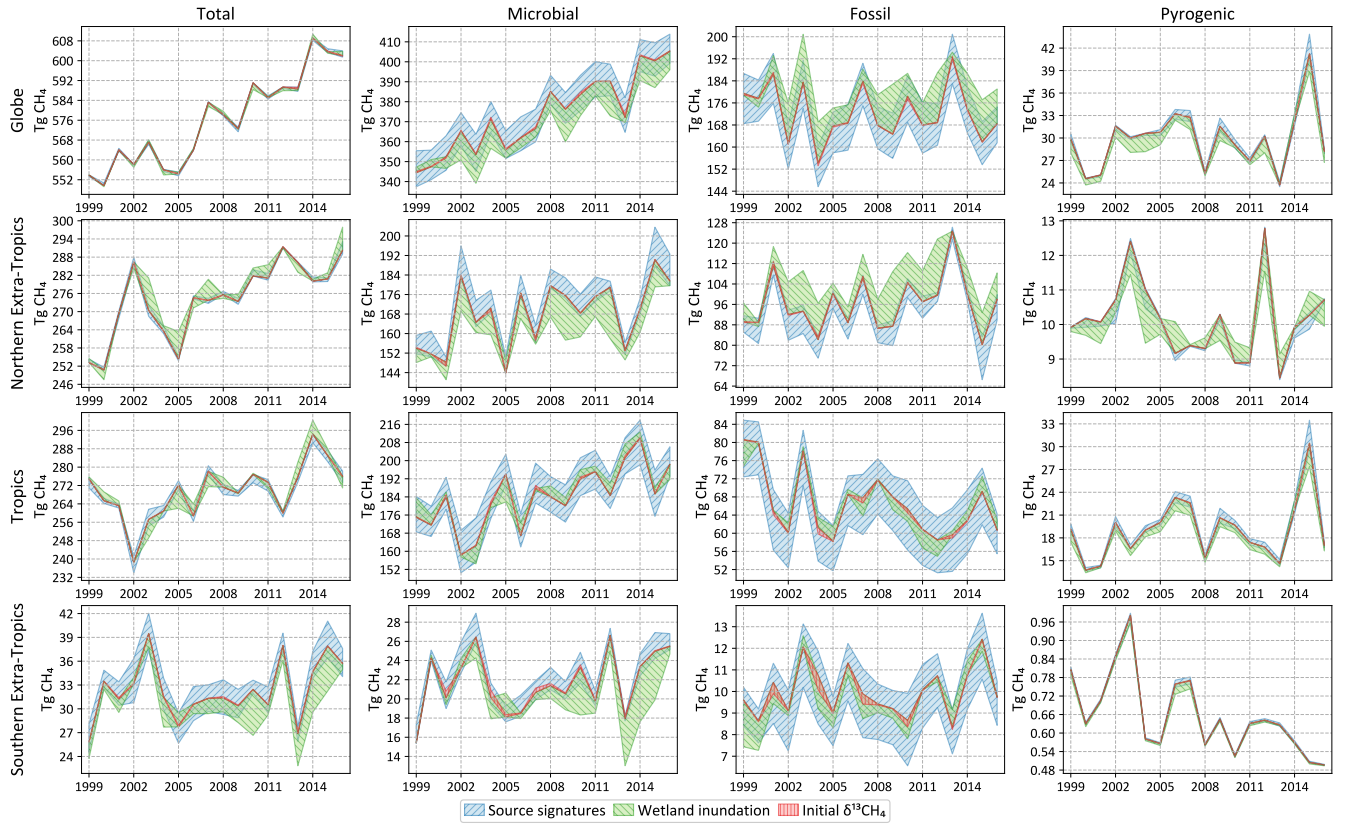
Figure 9. Total and source-specific annual emissions of CH$_4$ globally and from three latitudinal bands as in Figure 7. The shaded regions denote the spread (max to min) of annual emissions from sensitivity tests described in § 2.6.3, § 2.6.4 and § 2.6.5.

Table 5. Average annual Monte Carlo-derived random uncertainty and possible bias in CH$_4$ emissions, separated by source type (Tot = total, Mic = microbial, Fos = fossil, Pyr = pyrogenic) and latitude bands as in Figure 7. For each source type and region, the mechanism behind the largest possible bias has been demarcated by highlighting the bias in red. The "MC-derived" numbers are 2σ posterior uncertainties, all other numbers represent the range between maximum and minimum estimates. All numbers are in Tg CH$_4$ per year.

Region	Globe				N. Extra-Tropics				Tropics				S. Extra-Tropics			
Source type	Tot	Mic	Fos	Pyr	Tot	Mic	Fos	Pyr	Tot	Mic	Fos	Pyr	Tot	Mic	Fos	Pyr
MC-derived (2σ)	3.8	13.1	13.5	2.9	9.5	13.7	12.9	1.5	10.7	12.9	10.4	2.3	4.3	5.0	2.9	0.2
Tropospheric chlorine	0.6	26.3	25.9	0.2	4.8	20.1	15.1	0.2	3.4	7.3	10.6	0.2	1.6	1.4	0.3	0.0
OH fractionation	1.5	42.1	41.4	0.8	1.7	10.5	11.9	0.1	3.0	29.2	26.1	0.6	1.3	2.5	3.4	0.0
Source signatures	1.1	16.3	16.2	1.0	1.8	8.8	8.2	0.2	4.1	16.3	12.3	1.2	3.5	2.1	2.6	0.0
Wetland inundation	1.0	9.3	10.1	1.3	3.5	8.9	10.6	0.6	3.7	4.6	2.3	1.1	2.5	2.1	0.7	0.0
Initial δ^{13}CH$_4$	0.1	0.5	0.4	0.0	0.1	0.4	0.4	0.0	0.1	0.4	0.4	0.0	0.1	0.2	0.1	0.0

previous inversion's fifth year mole fraction field as initial condition. The last year of each inversion is discarded in the end, and the first five years' fluxes are stitched together and analyzed.

The posterior uncertainties of the emissions derived from this modified setup are calculated by performing a Monte-Carlo suite of 100 inversion as described in § 2.6. The Monte-Carlo runs follow the geometry of Figure 2(b) as well, with the ith inversion (i = 1 to 100) of each period initialized from the 5th year mole fraction field of the ith inversion of the previous period. This allows us to calculate not only annual uncertainties but also uncertainties on long term averages.

To study the transition around 2007, we considered two periods 2000–2006 and 2008–2014. Average total and source-specific emissions over the two periods are shown in Figure 10, as well as the change in the average emissions between the two periods. The prior fluxes do not change between the two periods, therefore the estimated change must be driven by the atmospheric observations. Both the CH_4-only and the $CH_4 + \delta^{13}CH_4$ inversions estimate a change in the total emission of $(27.1 \pm 0.6)\,\mathrm{Tg\,yr^{-1}}$ to match the increase in the atmospheric burden. However, while the CH_4-only inversion attributes $\sim 70\,\%$ of that to fossil CH_4 emissions and only $\sim 29\,\%$ to microbial emissions, the addition of $\delta^{13}CH_4$ data switches the balance to $\sim 15\,\%$ fossil and $\sim 85\,\%$ microbial. This change in the allocation of the methane emission in the presence of $\delta^{13}CH_4$ data is significant compared to the uncertainties on the changes as depicted in Figure 10. The contribution of pyrogenic emissions to the change is small in both inversions, and its change between the two inversions is not significant compared to its uncertainty. This is consistent with the downward trend in the global average $\delta^{13}CH_4$ in Figure 1, since microbial sources are the lightest of the three source types.
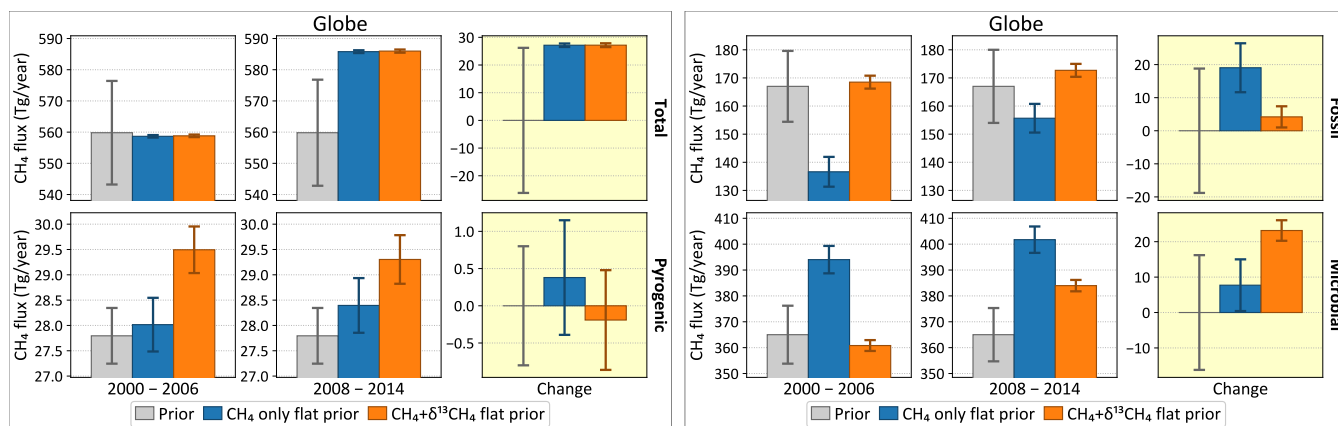
Figure 10. Change in global CH_4 emissions between the periods 2000–2006 and 2008–2014, total (top left) and disaggregated by source type. The gray bars denote prior emissions, and the colored bars denote two inversions, one with and the other without assimilated $\delta^{13}CH_4$ data. For each source type, the first two columns show the average emission over the two periods in question, and the third column shows the change between the two periods. The 1σ error bars are derived from a 100-member Monte Carlo ensemble of inversions following the configuration of Figure 2(b).

Geographically, the change between the two periods is driven almost equally by the Tropics and the northern extra-Tropics (Figure 11). In the Tropics, the addition of $\delta^{13}CH_4$ data results in higher microbial emissions in both periods. The change
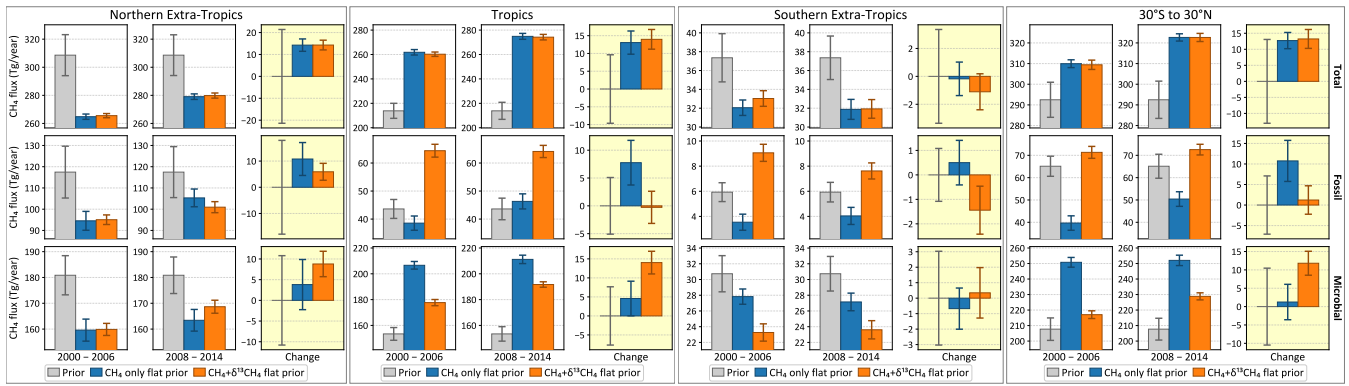
Figure 11. Similar to Figure 10, but disaggregated into different latitude bands. As in Figure 7, "Tropics" refers to the region between 23.5 °S and 23.5 °N. Pyrogenic emissions have not been plotted because of their small contribution in all ~~three~~ latitude bands.

between the two periods is also attributed to microbial emissions, unlike a CH_4-only inversion which attributes the change
primarily to fossil methane. In the northern extra-Tropics, although the presence of $\delta^{13}CH_4$ data point to increase in microbial emissions between the two periods, the relative apportionment of the increase between fossil and microbial emissions does not differ significantly from the CH_4-only emission if we consider the respective uncertainty estimates. ~~This suggests that the~~ Therefore, the largest contribution to the global increase in microbial emissions between the two periods (Figure 10) ~~is driven largely by~~ comes from the Tropics.

It is worth noting here that a change in emission strengths is not the only possible mechanism for an increase in atmospheric CH_4; a reduction in the sink strength could also induce a positive trend in atmospheric CH_4 post-2007. However, Lan et al. (2021) have shown that the changes in sinks proposed so far in the literature to explain the post-2007 CH_4 growth are not consistent with the observed $\delta^{13}CH_4$ trend post-2007. We therefore do not consider those alternatives here.

3.5 Separating microbial and fossil emissions

The CH_4 observations assimilated in a CH_4-only inversion constrain the total CH_4 emission, and any source disaggregation relies on spatiotemporal separation of emissions as encoded in the prior emissions and their uncertainties. Since the two largest CH_4 source types, microbial and fossil, have different $\delta^{13}CH_4$ source signatures, assimilating $\delta^{13}CH_4$ observations should provide additional information to separate the two sources compared to a CH_4-only inversion. We can evaluate this additional information by looking at the posterior correlation between microbial and fossil emissions, both globally and regionally. Posterior correlations between global annual microbial and fossil CH_4 emissions, calculated from our 100-member ensemble of independent inversions as described in § 2.6, are shown in Figure ~~12~~12. Error bars on the correlations shown in Figure ~~12~~12 represent the 95th percentile range of 20,000 evaluations of the correlation by randomly sampling the 100-member inversion ensemble with replacement (Efron and Tibshirani, 1994).

~~Posterior correlation between global annual microbial and fossil CH_4 emissions for the two inversions of Figure 7.~~
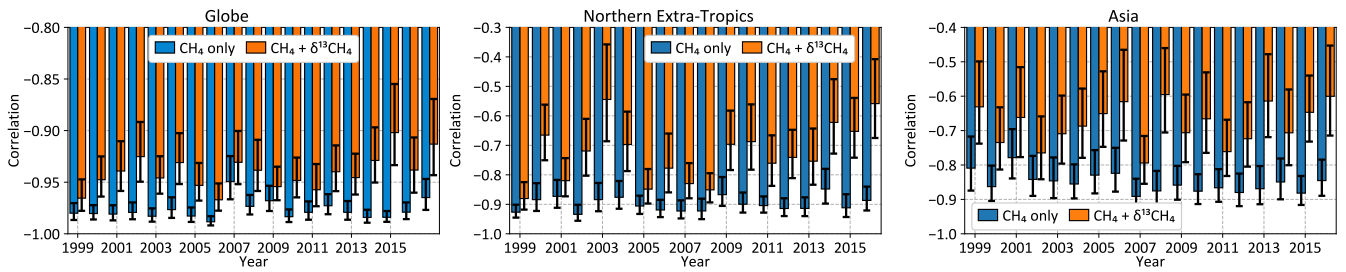
Figure 12. Posterior correlation between global annual microbial and fossil CH$_4$ emissions (left), and over the Northern Extra-Tropics (~~left~~center) and Asia (right) for the two inversions of Figure 7.

For all the years shown in Figure ~~12~~12, a CH$_4$-only inversion results in a strong negative correlation between global microbial and fossil emissions, consistent with the idea that atmospheric CH$_4$ measurements constrain the total CH$_4$ budget much better than individual source types. The addition of δ^{13}CH$_4$ data reduces this negative correlation, implying that δ^{13}CH$_4$ provides additional information to disentangle different CH$_4$ source types. The degree of disentanglement, represented by the reduction in the negative correlation, is determined by the δ^{13}CH$_4$ measurement coverage in a particular year and atmospheric transport connecting the emissions to those measurements. The correlation reduction is limited in our inversions by the relative sparsity of δ^{13}CH$_4$ measurements; even in the most recent 2012–2017 inversion period, only $2.8\,\%$ of CH$_4$ measurements have corresponding δ^{13}CH$_4$ measurements, overwhelmingly in locations far removed from significant CH$_4$ emissions (Figure 3). Having more δ^{13}CH$_4$ measurements in general, and specifically closer to emissive regions, should allow further disentangling of the different CH$_4$ source types.

Over smaller regions, only the Northern Extra-Tropics and Asia show significant decorrelation between annual fossil and microbial emissions (Figure ~~13~~12, center and right) with the addition of δ^{13}CH$_4$ data. While several other regions show similar reductions, the reductions are typically not significant compared to the 95$^{\text{th}}$ percentile error bars. The significant decorrelation seen for Northern Extra-Tropical and Asian emissions may be because most δ^{13}CH$_4$ measurements are in the Northern Extra-Tropics and downwind of Asia in the Pacific. To see similar significant decorrelation over other regions we will likely need increased δ^{13}CH$_4$ coverage closer to those regions. Although Figure 3 shows some δ^{13}CH$_4$ measurements over North America and Europe, the majority of those measurements are from the background air sampling sites Niwot Ridge and Jungfraujoch respectively, and therefore do not contribute to significant decorrelation of fossil and microbial emissions from those continents.

3.6 ~~Comparison to the GCP methane budget~~

~~The Global Carbon Project (GCP) periodically publishes top-down and bottom-up budgets of methane emissions from a suite of models. However, a meaningful comparison between our emissions and the 2020 GCP budget is not straightforward. The GCP bottom-up (BU) budget for 2008–2017, with emissions and sinks, significantly overestimates the atmospheric growth rate. This is primarily due to an overestimate of both microbial (freshwater sources) and fossil (geologic sources) methane in the GCP budget, making a direct comparison with our microbial and fossil estimates meaningless. The GCP top-down~~

470 (TD) estimates do not provide a fossil-microbial split of "other natural" emissions, also making a direct comparison with our estimates difficult. However, it is possible to calculate emissions for certain GCP categories from our inversions for some limited comparisons.

Assuming that methane from geological seeps do not change significantly over decadal time scales, we subtract geologic methane from our fossil methane emissions to estimate fossil fuel emissions for both the 2000–2009 and 2008–2016 periods, with a change of between the two periods. This is in stark contrast with GCP BU estimates of and for the two periods respectively. The GCP TD fossil fuel estimates for the two periods are and respectively, lower than both our estimates and the GCP BU estimates. While our baseline estimates for the two periods may be influenced by systematic biases (§ 2.6), the change between the two periods is relatively robust. With the alternate specification of tropospheric chlorine and alternate fractionation due to the OH oxidation , the two biggest sources of bias in source apportionment by , the change in our fossil fuel emission estimate between the two periods is and respectively, well within our uncertainty estimate of and significantly lower than both the GCP BU and the GCP TD estimates. The GCP BU (TD) estimate of an increase of () between the two periods is closer to our estimate of from a CH$_4$-only inversion, but not when data are incorporated.

For reasons mentioned above, we cannot directly compare our microbial emission estimates to GCP emission estimates. However, if we assume that methane from termites, wild animals and oceans do not change over decadal time scales, we can compare the change in the GCP TD estimate of wetlands, agriculture and waste from 2000–2009 to 2008–2016 with the change of microbial emissions in our inversion estimates. The GCP TD budget estimates a change of between those two periods, compared to our estimate of from a joint and CH$_4$ inversion and of from a CH$_4$-only inversion. Thus, the change in microbial emissions in the GCP TD budget is at the lower end of but consistent with our estimate from a CH$_4$-only emission, while it is not consistent with our budget after incorporating data. We cannot perform a similar analysis with the GCP BU budget because freshwater emissions cannot be assumed to be static over decadal time scales.

Finally, our pyrogenic emission estimates for both 2000–2009 and 2008–2016 periods are , with a change of . These are close to the GCP BU (TD) estimates of and (and) respectively. Neither the GCP budgets nor our inversion show significant changes in pyrogenic methane emissions between the two periods.

4 Conclusions and discussion

We have constructed a variational atmospheric inversion system capable of assimilating CH$_4$ and δ^{13}CH$_4$ measurements to estimate source-specific methane emissions within the TM5 4DVAR framework. We have assimilated CH$_4$ and δ^{13}CH$_4$ measurements from a multi-agency air sampling network in this framework to estimate fossil, microbial and pyrogenic emissions of atmospheric CH$_4$ globally. We have derived Bayesian uncertainty estimates on our emissions (random error), as well as investigated the impact of biases from non-optimized aspects of our inversion (systematic error). Our conclusions can be summarized as follows. In § 4.1 we summarize the main lessons learned from our work. In § 4.2 to 4.5 we compare our work and results with several other estimates in the literature. In § 4.6, we outline several planned additions and improvements to

our framework in the future. Finally, in § 4.7 we present areas of progress that we think are required in order to better use atmospheric $\delta^{13}CH_4$ data to disentangle the methane budget.

4.1   Enumerated conclusions

First, Figures 5 and 6 show that our inversion assimilating only CH_4 does not yield a CH_4 emission distribution consistent with atmospheric $\delta^{13}CH_4$. This is very likely true of CH_4 inversions in general, since they have no constraints forcing them to match atmospheric $\delta^{13}CH_4$ gradients and trends. Starting from a prior emission distribution consistent with atmospheric $\delta^{13}CH_4$ trends does not ensure that the posterior emission estimates will remain consistent. Our CH_4-only inversion started from a prior that reproduced the global mean atmospheric $\delta^{13}CH_4$ trend (scenario "C_WL+" of Lan et al., 2021), yet the posterior deviated from it as shown in Figures 5 and 6. We conclude that the only way to guarantee a posterior emission distribution consistent with both atmospheric CH_4 and $\delta^{13}CH_4$ data is to assimilate them simultaneously.

Second, given an atmospheric sink scenario, our current observational coverage allows us to estimate the global total CH_4 emission with a 2σ random uncertainty of $\sim 3.8\,\mathrm{Tg\,yr^{-1}}$, which is less than $1\,\%$ of the total emission. Microbial, fossil and pyrogenic emission uncertainties are around $3.5\,\%$, $8\,\%$ and $10\,\%$ respectively at the global scale. Given these posterior uncertainties, there are significant differences between inversions with and without $\delta^{13}CH_4$ data in the apportionment of the total CH_4 emission between microbial and fossil sources, both globally and in the Tropics (Figure 7 and Table 4). In both regions, the inclusion of $\delta^{13}CH_4$ data in an inversion results in a significantly higher proportion of fossil emissions compared to microbial emissions, which we consider realistic since it matches both atmospheric CH_4 and $\delta^{13}CH_4$ data (Figures 4 and 5). Pyrogenic emissions are relatively insensitive to the inclusion of $\delta^{13}CH_4$ data.

Third, we tested the sensitivity of our results to several factors that can lead to biases or systematic errors, as detailed in § 2.6. This included different maps of the $\delta^{13}CH_4$ isotopic source signatures, static and dynamic maps of the wetland inundation extent, different initial $\delta^{13}CH_4$ fields, different fractionation factors for the $CH_4 + OH$ oxidation mechanism, and different fields of tropospheric Cl. The last two factors had by far the largest impacts on the large scale apportionment between microbial and fossil emissions, even though their impact on the total CH_4 budget was nil or negligible. With the OH fractionation of Cantrell et al. (1990), the global microbial emission increases to $414\,\mathrm{Tg\,yr^{-1}}$ and the fossil emission drops to $131\,\mathrm{Tg\,yr^{-1}}$. With the lower estimate of tropospheric Cl from Wang et al. (2021), the global microbial emission decreases to $345\,\mathrm{Tg\,yr^{-1}}$ while the fossil emission increases to $199\,\mathrm{Tg\,yr^{-1}}$. Since some CH_4 inversions in the literature do not simulate a tropospheric Cl sink of CH_4, we tested the impact of this limiting case as well. In the absence of a tropospheric Cl sink, the global microbial emission drops further to $331\,\mathrm{Tg\,yr^{-1}}$ and the fossil emission increases to $213\,\mathrm{Tg\,yr^{-1}}$. Most of these shifts in the global partitioning are accompanied by shifts in the latitudinal partitioning. All of these are significant revisions to the partitioning of Table 4, suggesting that the ability of atmospheric $\delta^{13}CH_4$ measurements to partition the total CH_4 emission into different source types, at least over large regions, is limited by our knowledge of these two critical chemical processes. The uncertainty in our knowledge of $\delta^{13}CH_4$ source signatures, long considered a limitation on the use of $\delta^{13}CH_4$ data, is almost never a leading driver of uncertainty in Table 5, although it is usually more significant than either inundation extent or the initial $\delta^{13}CH_4$ field.

Finally, our tests suggest that the impact of an incorrect initial $\delta^{13}CH_4$ field can be ameliorated by a relatively short spin-up of one year in an inversion, in contrast to a multi-decadal spin-up necessary for a forward model run.

Fourth, atmospheric $\delta^{13}CH_4$ data strongly suggest that the rise in microbial emissions is the primary driver of the post-2007 growth in atmospheric CH_4. While a CH_4-only inversion starting from priors without a time trend attributes $\sim 70\%$ of the growth to fossil emissions, the addition of $\delta^{13}CH_4$ data shifts that to microbial emissions being responsible for $\sim 85\%$ of the growth. Since the latter inversion is consistent with atmospheric $\delta^{13}CH_4$ data while the former is not (Figure 5), we consider a majority microbial contribution to the post-2007 growth to be more realistic. A disaggregation of the growth by latitude bands suggests that a significant majority of the increase in tropical methane emissions is due to microbial and not fossil emissions. Moreover, although some of the sensitivity tests of § 2.6 lead to different partitioning between microbial and fossil emissions, they all suggest a steeper trend in microbial compared to fossil emissions in Figures 8 and 9.

Fifth, the ability of $\delta^{13}CH_4$ data to disentangle different CH_4 source types can be quantified by the reduction in the posterior correlation between emissions from those sources owing to the addition of $\delta^{13}CH_4$ data, compared to a CH_4-only inversion. Considering the two largest source types of methane, microbial and fossil, we see significant reductions in their posterior correlation over the globe as well as the northern extra-tropics and Asia. The degree of decorrelation, however, is limited, and we do not see significant decorrelation over other regions. We hypothesize that this is not a limitation of our understanding of $\delta^{13}CH_4$ but rather of its limited observational coverage. Even in the most recent years less than 3% of assimilated CH_4 measurements were accompanied by $\delta^{13}CH_4$ measurements, almost exclusively from background sites. It is very likely that an increase in the observational coverage of $\delta^{13}CH_4$, preferably close to source regions, will improve the capability of $\delta^{13}CH_4$ measurements to distinguish between different CH_4 source types.

Sixth, while it is difficult to compare our emission budget directly with GCP due to different partitioning schemes, we note that our fossil fuel emissions for both the 2000–2009 and 2008–2016 periods are higher than the GCP top-down and bottom-up emissions. However, our estimate of the change in fossil fuel emissions between the two periods is significantly lower than the GCP estimates. Concurrently, our estimate of the change in microbial emissions over the same time is significantly higher than the GCP top-down estimate. Both of these discrepancies are driven by atmospheric $\delta^{13}CH_4$ data, since our CH_4-only inversion provides changes that are consistent with GCP estimates. We therefore conclude that the microbial and fossil emission change estimates in the GCP budget are consistent with atmospheric CH_4 data but not with $\delta^{13}CH_4$ data. Finally, our pyrogenic emission estimates are consistent with or close to the GCP estimates for both periods.

4.2 Comparison to the GCP methane budget

The Global Carbon Project (GCP) periodically publishes top-down and bottom-up budgets of methane emissions from a suite of models. However, a meaningful comparison between our emissions and the 2020 GCP budget (Saunois et al., 2020) is not straightforward. The GCP bottom-up (BU) budget for 2008–2017, with $737\,Tg\,yr^{-1}$ emissions and $625\,Tg\,yr^{-1}$ sinks, significantly overestimates the atmospheric growth rate. This is primarily due to an overestimate of both microbial ($159\,Tg\,yr^{-1}$ freshwater sources) and fossil ($45\,Tg\,yr^{-1}$ geologic sources) methane in the GCP budget, making a direct comparison with our microbial and fossil estimates meaningless. The GCP top-down (TD) estimates do not provide a fossil-microbial split of "other

natural" emissions, also making a direct comparison with our estimates difficult. However, it is possible to calculate emissions for certain GCP categories from our inversions for some limited comparisons. For the period 2000–2009, we compare directly
570 by computing the 2000–2009 average from our inversions shown in Figure 7. However, since our inversions stop in 2016 and Table 3 of Saunois et al. (2020) reports the 2008–2017 average, we first calculate the 2008–2016 mean from the GCP budget using their reported 2008–2017 mean and their 2017 emissions. For computing the GCP means quoted here, we use the spreadsheet at https://doi.org/10.18160/GCP-CH4-2019, which may result in small differences from the numbers quoted in Table 3 of Saunois et al. (2020) due to rounding.

575 Our estimate of fossil fuel CH_4 emissions is significantly higher than GCP estimates, consistent with earlier work by Schwietzke et al. (2016) on $\delta^{13}CH_4$-based source apportionment. Subtracting $35\,\mathrm{Tg\,yr^{-1}}$ of geologic emissions from our fossil emission estimates, we arrive at $(137 \pm 2)\,\mathrm{Tg\,yr^{-1}}$ of fossil fuel emissions during both the 2000–2009 and 2008–2016 periods, significantly higher than the GCP BU (TD) estimates of $111\,\mathrm{Tg\,yr^{-1}}$ and $127\,\mathrm{Tg\,yr^{-1}}$ ($99\,\mathrm{Tg\,yr^{-1}}$ and $109\,\mathrm{Tg\,yr^{-1}}$) respectively. Recent measurements of $^{14}CH_4$ in ice cores suggest that geologic methane emissions are much lower than we
580 have assumed, with an upper 95th percentile confidence limit of $5.4\,\mathrm{Tg\,yr^{-1}}$ and mean of $1.6\,\mathrm{Tg\,yr^{-1}}$ (Hmiel et al., 2020). If true, this would push our fossil fuel emission estimates even higher to $(170 \pm 2)\,\mathrm{Tg\,yr^{-1}}$, indicating a significant underestimate in the GCP budget.

Assuming that methane emissions from geological seeps do not change significantly over decadal time scales, we estimate a change of $(0 \pm 2)\,\mathrm{Tg\,yr^{-1}}$ in fossil fuel CH_4 emissions from 2000–2009 to 2008–2016. This is markedly different from the
585 BU (TD) GCP budget, which estimates an increase of $16\,\mathrm{Tg\,yr^{-1}}$ ($10\,\mathrm{Tg\,yr^{-1}}$) between the two periods. While our baseline estimates for the two periods may be influenced by systematic biases (§ 2.6), the change between the two periods is relatively robust. With the alternate specification of tropospheric chlorine (Wang et al., 2021) and alternate fractionation due to the OH oxidation (Cantrell et al., 1990), the two biggest sources of bias in source apportionment by $\delta^{13}CH_4$, the change in our fossil fuel emission estimate between the two periods is $1\,\mathrm{Tg\,yr^{-1}}$ and $-1.7\,\mathrm{Tg\,yr^{-1}}$ respectively, well within our uncertainty
590 estimate of $2\,\mathrm{Tg\,yr^{-1}}$ and significantly lower than both the GCP BU and the GCP TD estimates. The GCP BU (TD) estimate of an increase of $16\,\mathrm{Tg\,yr^{-1}}$ ($10\,\mathrm{Tg\,yr^{-1}}$) between the two periods is closer to our estimate of $(8.4 \pm 5.6)\,\mathrm{Tg\,yr^{-1}}$ from a CH_4-only inversion, which is not consistent with $\delta^{13}CH_4$ data.

For reasons mentioned above, we cannot directly compare our microbial emission estimates to GCP emission estimates. However, if we assume that methane from termites, wild animals and oceans do not change over decadal time scales, we can
595 compare the change in the GCP TD estimate of wetlands, agriculture and waste from 2000–2009 to 2008–2016 with the change of microbial emissions in our inversion estimates. The GCP TD budget estimates a change of $12.6\,\mathrm{Tg\,yr^{-1}}$ between those two periods, compared to our estimate of $(26 \pm 2)\,\mathrm{Tg\,yr^{-1}}$ from a joint $\delta^{13}CH_4$ and CH_4 inversion and of $(18 \pm 6)\,\mathrm{Tg\,yr^{-1}}$ from a CH_4-only inversion. Thus, the change in microbial emissions in the GCP TD budget is at the lower end of but consistent with our estimate from a CH_4-only emission, while it is not consistent with our budget after incorporating $\delta^{13}CH_4$ data. We cannot
600 perform a similar analysis with the GCP BU budget because freshwater emissions cannot be assumed to be static over decadal time scales.

Finally, our pyrogenic emission estimates for both 2000–2009 and 2008–2016 periods are $(30.0 \pm 0.6)\,\mathrm{Tg\,yr^{-1}}$, with a change of $(0.3 \pm 0.5)\,\mathrm{Tg\,yr^{-1}}$. These are close to the GCP BU (TD) estimates of $31\,\mathrm{Tg\,yr^{-1}}$ and $30\,\mathrm{Tg\,yr^{-1}}$ ($29\,\mathrm{Tg\,yr^{-1}}$ and $31\,\mathrm{Tg\,yr^{-1}}$) respectively. Neither the GCP budgets nor our inversion show significant changes in pyrogenic methane emissions
605   between the two periods.

4.3   Comparison with Zhang et al. (2021b)

Zhang et al. (2021b) derive sector-specific changes in methane emissions from a two-box model by first creating an ensemble of emission scenarios consistent with known emissions of methane and their uncertainties, then comparing the resultant hemispheric mean CH_4 and $\delta^{13}CH_4$ in the atmosphere with measurements. Based on the ensemble members that agree with
610   hemispheric mean CH_4 and $\delta^{13}CH_4$ time series, they come up with sector-specific emission changes. We note here that according to Figures 1B and 2A of Zhang et al. (2021b), none of their choices fit the atmospheric $\delta^{13}CH_4$ data very well. We hypothesize that this is due both to the biases in their bottom-up emission estimates which could not be sufficiently corrected due to tight assumed uncertainties on them, and the inability of a box model to interpret spatial gradients of CH_4 and $\delta^{13}CH_4$. Specifically, Figure 1B of Zhang et al. (2021b) shows that none of the ensemble members can reproduce the recent downward trend in
615    $\delta^{13}CH_4$. Therefore, their estimated fractional contribution of microbial (fossil) emissions to the recent growth in CH_4 is likely to be too low (high).

Table 6. Comparison of the attribution of the recent growth of atmospheric CH_4 between Zhang et al. (2021b) and this work. The numbers show the change in emissions from a baseline period of 2000–2006 to two different periods, 2007–2012 and 2013–2017. All numbers are in Tg CH_4 per year. Uncertainties on the Zhang et al. (2021b) estimates obtained by personal communication with Zhen Zhang.

Source type	2007–2012		2013–2017	
	Zhang et al. (2021b)	This work	Zhang et al. (2021b)	This work
Total	31.7 ± 9.0	23.1 ± 0.8	45.3 ± 10.2	41.6 ± 0.7
Microbial	23.9 ± 5.1	25.5 ± 3.1	29.0 ± 1.9	32.3 ± 3.2
Fossil	10.5 ± 7.2	-2.5 ± 3.5	17.5 ± 10.0	9.2 ± 3.5
Pyrogenic	-2.8 ± 0.3	0.0 ± 0.7	-1.2 ± 0.2	0.1 ± 0.8

Table 6 summarizes the changes in methane emissions from the "quasi-stable" period of 2000–2006 to two later periods during the renewed growth, 2007–2012 and 2013–2017. For both the periods, we estimate significantly smaller contributions from fossil emissions compared to Zhang et al. (2021b). While the microbial contributions look similar in magnitude, they
620   constitute a smaller fraction of the total change for Zhang et al. (2021b). Lastly, while Zhang et al. (2021b) estimate a downward trend in pyrogenic emissions, we do not estimate a trend significantly different from zero. To summarize, we estimate a larger (smaller) influence of increasing microbial (fossil) emissions behind the recent CH_4 growth, which is likely to be more accurate because it better reproduces the observed $\delta^{13}CH_4$ trend in the atmosphere (compare Figure 5 here with Figure 1B of Zhang et al.

(2021b)). We cannot separate the anthropogenic from natural microbial contributions in our framework, and we note that such a separation by Zhang et al. (2021b) relies on their modeled wetland fluxes and not on atmospheric CH_4 or $\delta^{13}CH_4$ data.

4.4 Comparison with Thanwerdas et al. (2021)

Thanwerdas et al. (2021) describe an alternative variational inversion framework using the LMDz-SACS model to assimilate CH_4 and $\delta^{13}CH_4$ measurements. We find it heartening that others have decided to tackle this complicated problem. Since they reserve decadal dual tracer inversions for future work, we will compare their technique with ours to highlight the similarities and differences. The biggest difference lies in the decision of Thanwerdas et al. (2021) to optimize $\delta^{13}CH_4$ source signatures, compared to our choice of keeping them fixed for a specific inversion. While $\delta^{13}CH_4$ source signatures are uncertain for many methane sources, we explain our reasons for not optimizing them in § 2.6.3. Instead, we explore the impact of source signature uncertainty with different constructions of the source signature map as detailed in § 2.6.3. In the end, at least for large geographical regions, the uncertainty from source signatures did not prove to be a leading uncertainty (Table 5). The second major difference between the two inversion frameworks lies in the construction of the prior CH_4 fluxes. While Thanwerdas et al. (2021) use a prior that approximately matches the atmospheric CH_4 growth rate, we construct our priors to match both the CH_4 growth rate and the $\delta^{13}CH_4$ trend over two decades. We suspect this, and the linearity of our formulation due to not optimizing source signatures, to be the reasons why our inversion required a shorter spin-up time compared to Thanwerdas et al. (2021).

There are also a few differences in implementation between the two frameworks. Most notably, Thanwerdas et al. (2021) estimate the posterior uncertainty as the spread between different inversion configurations, correctly stating that an evaluation of the posterior covariance matrix would require significantly more computing resources. We evaluate that posterior covariance matrix for both $CH_4 + \delta^{13}CH_4$ and CH_4-only inversions and present both types of uncertainty, namely the systematic uncertainty as the spread between multiple inversion configurations, and the random (Bayesian) uncertainty as the spread of an ensemble of 100 independent inversions. The configurations we explore for the systematic uncertainty are also different from Thanwerdas et al. (2021), and include alternate specifications of the Cl oxidant and the isotopic discrimination of the $CH_4 + OH$ reaction. We find the latter two to be the most significant drivers of uncertainty for partitioning CH_4 emissions using $\delta^{13}CH_4$ data.

While our implementation of the inversion is different from Thanwerdas et al. (2021), our goals are very similar. We look forward to long-term inversions of CH_4 and $\delta^{13}CH_4$ data using LMDz-SACS so that we may compare and contrast with our results presented here, and figure out how best to use isotopic measurements to solve the atmospheric methane puzzle.

4.5 ~~Future work~~ Comparison with other top-down studies using CH_4 and ~~outlook~~ $\delta^{13}CH_4$

In addition to the publications compared in detail above, some others have used combinations of CH_4 and $\delta^{13}CH_4$ observations to infer sector-specific sources of methane and the causes behind the recent increase, either in 2D (Thompson et al., 2018) or 3D (McNorton et al., 2018) atmospheric models. In terms of attributing the recent growth of CH_4, the most significant difference between our work and either of those studies is that our inferred change in biomass burning emissions is smaller. For example, our GFED 4.1s prior has a reduction of $1.35\,\mathrm{Tg\,yr^{-1}}$ in pyrogenic emissions from 2003–2006 to 2007–2015

(van der Werf et al., 2017). This is changed to a reduction of $0.81\,\mathrm{Tg\,yr^{-1}}$ by our $\mathrm{CH_4}+\delta^{13}\mathrm{CH_4}$ inversion (Figure 7), and to a reduction of $(0.19 \pm 0.72)\,\mathrm{Tg\,yr^{-1}}$ when we start from a prior without trends (Figure 10). This suggests that the estimate of reduced pyrogenic emissions is driven primarily by its presence in the prior and not by $\delta^{13}\mathrm{CH_4}$ data, which is sparse near regions with large fire emissions. To contrast, McNorton et al. (2018) infer a reduction of $2.9\,\mathrm{Tg\,yr^{-1}}$ in pyrogenic emissions between the same periods, allowing for a larger increase in fossil emissions to balance $\mathrm{CH_4}$ and $\delta^{13}\mathrm{CH_4}$ trends. Finally, we note that even though the "INV_FIXED" inversion of McNorton et al. (2018) with climatological priors allows for variations in OH and is therefore not directly comparable to our analogous inversion, their "INV_FIXED" estimates no reduction in pyrogenic emissions (Table 6 of McNorton et al., 2018). This supports our hypothesis that a reduction in pyrogenic emissions is driven primarily by the prior and not by atmospheric $\delta^{13}\mathrm{CH_4}$ data.

In agreement with our estimates, Thompson et al. (2018) also attribute the majority of the growth between 2007 and 2014 to microbial and not fossil sources. They infer a $(3 \pm 2)\,\mathrm{Tg\,yr^{-1}}$ reduction in pyrogenic emissions during that period, compared to a reduction of $0.58\,\mathrm{Tg\,yr^{-1}}$ inferred by our $\mathrm{CH_4}+\delta^{13}\mathrm{CH_4}$ inversion ($(0.50 \pm 1.66)\,\mathrm{Tg\,yr^{-1}}$ reduction if we start with a climatological prior). We note that our prior pyrogenic emission for 2014 is $3.45\,\mathrm{Tg\,yr^{-1}}$ *higher* than 2007, and a $\mathrm{CH_4}$-only inversion estimates an *increase* of $1.65\,\mathrm{Tg\,yr^{-1}}$ between the two years (Figure 7), therefore even the small reduction we estimate must be driven by $\delta^{13}\mathrm{CH_4}$ data. However, since this reduction is smaller than the $(3 \pm 2)\,\mathrm{Tg\,yr^{-1}}$ estimated by Thompson et al. (2018), our fossil emission increase is also smaller to balance the $\delta^{13}\mathrm{CH_4}$ trend. Finally, Thompson et al. (2018) do not estimate a significant role of the chemical sink behind the recent $\mathrm{CH_4}$ growth, consistent with our previous work (Lan et al., 2021).

4.6 Future work

While we feel confident in the $\mathrm{CH_4}$ emission estimates reported here, there are several areas which we plan to explore and improve in future work.

4.6.1 Alternate OH

The atmospheric $\mathrm{CH_4}$ budget is determined by the balance between its sources and sinks, the latter primarily driven by the OH radical. While there have been some efforts to optimize atmospheric OH in concert with $\mathrm{CH_4}$ emissions (e.g., Zhang et al., 2018, 2021a; Yin et al., 2021), we do not think in situ $\mathrm{CH_4}$ samples provide sufficient information to constrain the sink independently. Moreover, estimates of OH abundance and variability over the past decades, either from $\mathrm{CH_4}$ inversions (Yin et al., 2021) or otherwise (Bousquet et al., 2005; Montzka et al., 2011; Nicely et al., 2018), are consistent with a limited role of OH variability in recent trends in atmospheric $\mathrm{CH_4}$. This is why, similar to the vast majority of $\mathrm{CH_4}$ inversions, we have chosen to keep the OH sink fixed to a field consistent with observed trends and gradients of methyl chloroform (MCF, Spivakovsky et al., 2000; Patra et al., 2014, 2020). Nonetheless, we acknowledge that our knowledge of atmospheric OH is imperfect and uncertain, and in future work we plan to explore alternate specifications of OH that are consistent with our knowledge of atmospheric chemistry and MCF trends and gradients.

4.6.2 Alternate optimizer and source signature uncertainty

Errors in the specification of the $\delta^{13}CH_4$ source signatures can have significant impact on the inferred methane emissions (Thanwerdas et al., 2021). While we have explored alternate specifications, it is possible that the true uncertainty in $\delta^{13}CH_4$ source signatures is larger than the range we have explored. Optimizing the $\delta^{13}CH_4$ source signatures with a realistic prior covariance structure may yield larger but more realistic error bounds on source-specific methane emissions. We plan to explore that option in the future, which will require an alternate to the conjugate gradient optimizer (Lanczos, 1950) we currently use. We have tested the M1QN3 optimizer used by Thanwerdas et al. (2021), and have found its convergence to be slow and inefficient for our system. Therefore, we plan to explore and implement alternate optimizers that can work efficiently on non-linear problems, in order to have the option of estimating $\delta^{13}CH_4$ source signatures. Concurrently, we will work on a more complete characterization of the $\delta^{13}CH_4$ source signature uncertainty, which will be required in order to derive a prior error covariance matrix for $\delta^{13}CH_4$.

4.6.3 OSSEs

We have tested the ability of existing $\delta^{13}CH_4$ observations to infer mechanisms behind the recent CH_4 growth and separate different CH_4 source types, and found that the ability to distinguish fossil from microbial emissions – as reflected by the posterior correlation between them – is limited at policy-relevant scales (§ 3.5). We strongly suspect that this is a limitation of the existing $\delta^{13}CH_4$ observational coverage and not of the inversion technique. If we consider expanding the $\delta^{13}CH_4$ measurement network to improve that ability in the future, we need to quantify the added value of different expansion strategies. We plan to do this with Observation System Simulation Experiments (OSSEs) simulating different observational networks, as we have done for ^{14}C of CO_2 in the past (Basu et al., 2016).

4.6.4 Satellite CH_4 retrievals

Several satellites have been launched by various space agencies in the past decades to estimate atmospheric CH_4 from space, and several more are slated to go up over the next decade. As the technique to use $\delta^{13}CH_4$ in CH_4 inversions matures, we hope to eventually add satellite CH_4 data to such inversions to provide stronger regional constraints.

4.7 Future needs

While our effort to quantify source-specific methane emissions from atmospheric $\delta^{13}CH_4$ measurements has yielded several significant results, it has also uncovered areas for further progress. First, Figure 3 shows a lack of $\delta^{13}CH_4$ data over the Tropics and close to source regions. This is due to the historical choice of preferentially measuring $\delta^{13}CH_4$ at background sites and the general lack of Tropical samples. More $\delta^{13}CH_4$ measurements in historically under-sampled regions would let us better separate Tropical emissions and attribute continental emissions to specific sources. Second, while the soil sink has a small impact on CH_4-only studies, its impact on $\delta^{13}CH_4$ studies is large owing to the strong fractionation. Recent studies have suggested that the soil sink may be underestimated in current biogeochemical models (Oh et al., 2020) and may have trends due to a

changing climate (Ni and Groffman, 2018; Murguia-Flores et al., 2021), both aspects that need better characterization. Third, our knowledge of the OH fractionation of $^{13}CH_4$ and the distribution of tropospheric Cl are sources of significant uncertainty in partitioning methane sources using $\delta^{13}CH_4$ data (§ 3.3). There is a wide range of estimates for OH fractionation in the literature (Rust and Stevens, 1980; Cantrell et al., 1990; Saueressig et al., 2001; Whitehill et al., 2017), and an analogously wide range of distributions of tropospheric Cl (Allan et al., 2007; Hossaini et al., 2016; Gromov et al., 2018). The uncertainty on both of these need to be reduced in order to use $\delta^{13}CH_4$ data more effectively. Finally, while we have ruled out a sink-only explanation for the recent growth of methane (Lan et al., 2021), a small contribution from sink variations is possible. Since direct measurements of OH are few and far between, and atmospheric levels of MCF are too low for quantifying recent variations in OH, we need alternate ways of separating source and sink influences. One possibility is to use measurements of δD in methane to constrain the sink (Quay et al., 1999; Sowers, 2006; Whiticar and Schaefer, 2007). We plan to explore the potential of δD measurements in future work.

Code availability. TM5 4DVAR code for performing the inversions is publicly available at https://sourceforge.net/p/tm5/cy3_4dvar/ci/default/tree/.

Data availability. The CH_4 and $\delta^{13}CH_4$ data assimilated for this exercise can be downloaded from https://doi.org/10.15138/64w0-0g71.

Author contributions. SB built the extensions needed to TM5 4DVAR to assimilate CH_4 and $\delta^{13}CH_4$ data, and performed all model runs. SS and XL constructed prior flux and source signature maps. ED and SM provided CH_4 and $\delta^{13}CH_4$ data respectively, with expert advice on data errors and which datasets to assimilate. ED, SM, SS and XL constructed the multi-agency atmospheric data sets to be assimilated. KT collated all measurements into a common format for model use. SS obtained the initial grant for this study and designed the study protocols with the other co-authors. PPT and JBM provided expertise on interpreting $\delta^{13}CH_4$ measurements and the formulation of the isotope mass balance equations. LB provided expertise on the global methane budget. YO provided wetland CH_4 emissions and source signatures from the IsoTEM model. FA provided CH_4 data from Plateau de Rosa, Italy. LVG provided CH_4 data from multiple aircraft profiling sites in Brazil. AJ provided CH_4 and $\delta^{13}CH_4$ data from several sites maintained by the Max Planck Institute for Biogeochemistry, Jena. JN provided CH_4 data from Kasprowy Wierch, Poland. MS provided CH_4 and $\delta^{13}CH_4$ data from multiple surface sites, shipboard and aircraft sampling programs run by the National Institute for Environmental Studies, Japan. SM provided CH_4 and $\delta^{13}CH_4$ data from surface and shipboard sampling programs run by Tohoku University. TDI provided CH_4 data from several sampling sites in Italy. GM provided CH_4 data from Ispra, Italy. HL provided CH_4 data from Anmyeon-do, Korea. JA provided CH_4 data from Monte Cimone, Italy. The manuscript was primarily written by SB, with input from XL, ED, SM, SS, JBM and PPT.

Competing interests. The authors declare no competing interests.

Acknowledgements. This work was supported by funding from the National Aeronautics and Space Administration (NASA), grant NNX17AK20G. All computing work was performed on either NASA's Discover supercomputer at the NASA Center for Climate Simulation (NCCS) or NOAA's Orion supercomputer maintained by the Mississippi State University. SB was additionally supported by NASA's Modeling, Analysis and Prediction and Carbon Monitoring System Programs. XL was supported in part by cooperative agreement NA17OAR4320101 between NOAA and the University of Colorado at Boulder. In addition to the coauthors who provided atmospheric CH_4 and $\delta^{13}CH_4$ measurements, the authors acknowledge the work of (i) Ove Hermansen, Cathrine Lund Myhre, and Stephen Platt of the Norwegian Institute for Air Research (NILU) in collecting air samples at the Zeppelin Observatory through Norwegian Environment Agency grant 21087006, ICOS Norway, Research Council of Norway grant 296012, and ReGAME, Research Council of Norway grant 325610; (ii) Heiko Moosen and Willi A. Brand of the Max Planck Institute for Biogeochemistry, funded by the Max Planck Society; (iii) Doug Worthy of Environment Climate Change Canada; (iv) Casper Labuschagne of the South African Weather Service; (v) László Haszpra of the Hungarian Meteorological Service; (v) Yosuke Niwa and Taku Umezawa of the National Institute for Environmental Studies, Japan; (vi) Shinya Takatsuji of the Japan Meteorology Agency for CH_4 measurements at Ryori, Yonagunijima, Minamitorishima and from JMA's "Aircraft Observation of Atmospheric trace gases" program; (vii) Arlyn Andrews, Bianca Baier, Molly Crotwell, Philip Handley, Jack Higgs, Jon Kofler, Pat Lang, Thomas Legard, Kathryn McKain, Eric Moglia, Don Neff, Tim Newberger, Colm Sweeney, and Sonja Wolter for support of the NOAA GGGRN tower and aircraft programs; (viii) Nina Paramonova of the Voeikov Main Geophysical Observatory, Russia; (ix) Dagmar Kubistin of the Deutscher Wetterdienst (DWD); (x) Karin Uhse and Ludwig Ries of the Umwelt Bundesamt, Germany; (xi) Juha Hatakka of the Finnish Meterological Institute; (xii) Emilio Cuevas of the Meteorological State Agency of Spain (AEMET); (xiii) Alex Vermeulen of Lund University; and (xiv) John Moncrieff of the University of Edinburgh. The authors also acknowledge atmospheric data provided by the National Institute of Water and Atmospheric Research (NIWA) of New Zealand, the Commonwealth Scientific and Industrial Research Organisation (CSIRO) of Australia, Laboratoire des Sciences du Climat et de l'Environnement (LSCE) of France, and the Swiss Federal Laboratories for Materials Science and Technology (EMPA). We also thank Martin Steinbacher (EMPA) for comments on the manuscript. NIWA measurements at Arrival Heights and Baring Head were supported by internal funding under Climate and Atmosphere Research Programme CAAC2204 (2021/22 SCI). EMPA measurements at Jungfraujoch were supported by the Swiss National Air Pollution Monitoring Network, the Federal Office for the Environment and ICOS Switzerland (Swiss National Science Foundation, grant 20FI21_148992). RSE contribution to this work has been financed by the Research Fund for the Italian Electrical System under the Contract Agreement between RSE S.p.A. and the Ministry of Economic Development – General Directorate for the Electricity Market, Renewable Energy and Energy Efficiency, Nuclear Energy in compliance with the Decree of April 16th, 2018.

References

Allan, W., Struthers, H., and Lowe, D. C.: Methane Carbon Isotope Effects Caused by Atomic Chlorine in the Marine Boundary Layer: Global Model Results Compared with Southern Hemisphere Measurements, Journal of Geophysical Research: Atmospheres, 112, n/a–n/a, https://doi.org/10.1029/2006JD007369, 2007.

Andrews, A. E., Kofler, J. D., Trudeau, M. E., Williams, J. C., Neff, D. H., Masarie, K. A., Chao, D. Y., Kitzis, D. R., Novelli, P. C., Zhao, C. L., Dlugokencky, E. J., Lang, P. M., Crotwell, M. J., Fischer, M. L., Parker, M. J., Lee, J. T., Baumann, D. D., Desai, A. R., Stanier, C. O., De Wekker, S. F. J., Wolfe, D. E., Munger, J. W., and Tans, P. P.: CO_2, CO, and CH_4 Measurements from Tall Towers in the NOAA Earth System Research Laboratory's Global Greenhouse Gas Reference Network: Instrumentation, Uncertainty Analysis, and Recommendations for Future High-Accuracy Greenhouse Gas Monitoring Effo, Atmospheric Measurement Techniques, 7, 647–687, https://doi.org/10.5194/amt-7-647-2014, 2014.

Basu, S., Guerlet, S., Butz, A., Houweling, S., Hasekamp, O., Aben, I., Krummel, P., Steele, P., Langenfelds, R., Torn, M., Biraud, S., Stephens, B., Andrews, A., and Worthy, D.: Global CO_2 Fluxes Estimated from GOSAT Retrievals of Total Column CO_2, Atmospheric Chemistry and Physics, 13, 8695–8717, https://doi.org/10.5194/acpd-13-4535-2013, 2013.

Basu, S., Krol, M., Butz, A., Clerbaux, C., Sawa, Y., Machida, T., Matsueda, H., Frankenberg, C., Hasekamp, O. P., and Aben, I.: The Seasonal Variation of the CO_2 Flux over Tropical Asia Estimated from GOSAT, CONTRAIL, and IASI, Geophysical Research Letters, 41, 1809–1815, https://doi.org/10.1002/2013GL059105, 2014.

Basu, S., Miller, J. B., and Lehman, S.: Separation of Biospheric and Fossil Fuel Fluxes of CO_2 by Atmospheric Inversion of CO_2 and $\Delta^{14}CO_2$ Measurements: Observation System Simulations, Atmospheric Chemistry and Physics, 16, 5665–5683, https://doi.org/10.5194/acp-16-5665-2016, 2016.

Basu, S., Lehman, S. J., Miller, J. B., Andrews, A. E., Sweeney, C., Gurney, K. R., and Tans, P. P.: Estimating US Fossil Fuel CO_2 Emissions from Measurements of ^{14}C in Atmospheric CO_2, Proceedings of the National Academy of Sciences, pp. 1–8, https://doi.org/10.1073/pnas.1919032117, 2020.

Bergamaschi, P., Houweling, S., Segers, A., Krol, M., Frankenberg, C., Scheepmaker, R. A., Dlugokencky, E., Wofsy, S. C., Kort, E. A., Sweeney, C., Schuck, T., Brenninkmeijer, C., Chen, H., Beck, V., and Gerbig, C.: Atmospheric CH_4 in the First Decade of the 21st Century: Inverse Modeling Analysis Using SCIAMACHY Satellite Retrievals and NOAA Surface Measurements, Journal of Geophysical Research: Atmospheres, 118, 7350–7369, https://doi.org/10.1002/jgrd.50480, 2013.

Bousquet, P., Hauglustaine, D. A., Peylin, P., Carouge, C., and Ciais, P.: Two Decades of OH Variability as Inferred by an Inversion of Atmospheric Transport and Chemistry of Methyl Chloroform, Atmospheric Chemistry and Physics, 5, 2635–2656, https://doi.org/10.5194/acp-5-2635-2005, 2005.

Bousquet, P., Ciais, P., Miller, J. B., Dlugokencky, E. J., Hauglustaine, D. A., Prigent, C., Van der Werf, G. R., Peylin, P., Brunke, E.-G., Carouge, C., Langenfelds, R. L., Lathière, J., Papa, F., Ramonet, M., Schmidt, M., Steele, L. P., Tyler, S. C., and White, J.: Contribution of Anthropogenic and Natural Sources to Atmospheric Methane Variability, Nature, 443, 439–443, https://doi.org/10.1038/nature05132, 2006.

Bousserez, N., Henze, D. K., Perkins, A., Bowman, K. W., Lee, M., Liu, J., Deng, F., and Jones, D. B. A.: Improved Analysis-Error Covariance Matrix for High-Dimensional Variational Inversions: Application to Source Estimation Using a 3D Atmospheric Transport Model, Quarterly Journal of the Royal Meteorological Society, 141, n/a–n/a, https://doi.org/10.1002/qj.2495, 2015.

Burkholder, J. B., Sander, S. P., Abbatt, J. P. D., Barker, J. R., Cappa, C., Crounse, J. D., Dibble, T. S., Huie, R. E., Kolb, C. E., Kurylo, M. J., Orkin, V. L., Percival, C. J., Wilmouth, D. M., and Wine, P. H.: Chemical Kinetics and Photochemical Data for Use in Atmospheric Studies, Evaluation No. 19, Tech. Rep. 19-5, Jet Propulsion Laboratory, Pasadena, CA, http://jpldataeval.jpl.nasa.gov/, 2019.

Cantrell, C. A., Shetter, R. E., McDaniel, A. H., Calvert, J. G., Davidson, J. A., Lowe, D. C., Tyler, S. C., Cicerone, R. J., and Greenberg, J. P.: Carbon Kinetic Isotope Effect in the Oxidation of Methane by the Hydroxyl Radical, Journal of Geophysical Research: Atmospheres, 95, 22 455–22 462, https://doi.org/10.1029/JD095iD13p22455, 1990.

Cerling, T. E., Ehleringer, J. R., and Harris, J. M.: Carbon Dioxide Starvation, the Development of C4 Ecosystems, and Mammalian Evolution, Philosophical Transactions of the Royal Society of London. Series B: Biological Sciences, 353, 159–171, https://doi.org/10.1098/rstb.1998.0198, 1998.

Chang, J., Peng, S., Ciais, P., Saunois, M., Dangal, S. R. S., Herrero, M., Havlík, P., Tian, H., and Bousquet, P.: Revisiting Enteric Methane Emissions from Domestic Ruminants and Their δ^{13}C-CH$_4$ Source Signature, Nature Communications, 10, 3420, https://doi.org/10.1038/s41467-019-11066-3, 2019.

Courtier, P., Andersson, E., Heckley, W., Pailleux, J., Vasiljević, D., Hamrud, M., Hollingsworth, A., Rabier, F., and Fisher, M.: The ECMWF Implementation of Three-Dimensional Variational Assimilation (3D-Var). I: Formulation, Quarterly Journal of the Royal Meteorological Society, 124, 1783–1807, http://www.ncbi.nlm.nih.gov/pubmed/10321055, 1998.

Craig, H.: Isotopic Standards for Carbon and Oxygen and Correction Factors for Mass-Spectrometric Analysis of Carbon Dioxide, Geochimica et Cosmochimica Acta, 12, 133–149, https://doi.org/10.1016/0016-7037(57)90024-8, 1957.

Crotwell, A. M., Lee, H., and Steinbacher, M.: 20th WMO/IAEA Meeting on Carbon Dioxide, Other Greenhouse Gases and Related Measurement Techniques (GGMT-2019), Tech. Rep. 255, World Meteorological Organization/Global Atmospheric Watch, Jeju Island, South Korea, https://library.wmo.int/index.php?lvl=notice_display&id=21758#.YkiLcpPMIUA, 2020.

Dlugokencky, E. J., Houweling, S., Bruhwiler, L., Masarie, K. A., Lang, P. M., Miller, J. B., and Tans, P. P.: Atmospheric Methane Levels off: Temporary Pause or a New Steady-State?, Geophysical Research Letters, 30, https://doi.org/10.1029/2003GL018126, 2003.

Dlugokencky, E. J., Myers, R. C., Lang, P. M., Masarie, K. A., Crotwell, A. M., Thoning, K. W., Hall, B. D., Elkins, J. W., and Steele, L. P.: Conversion of NOAA Atmospheric Dry Air CH$_4$ Mole Fractions to a Gravimetrically Prepared Standard Scale, Journal of Geophysical Research: Atmospheres, 110, https://doi.org/10.1029/2005JD006035, 2005.

Dlugokencky, E. J., Nisbet, E. G., Fisher, R., and Lowry, D.: Global Atmospheric Methane: Budget, Changes and Dangers, Philosophical Transactions of the Royal Society A: Mathematical, Physical and Engineering Sciences, 369, 2058–2072, https://doi.org/10.1098/rsta.2010.0341, 2011.

Efron, B. and Tibshirani, R. J.: An Introduction to the Bootstrap, Chapman and Hall/CRC, 1994.

Etiope, G., Ciotoli, G., Schwietzke, S., and Schoell, M.: Gridded Maps of Geological Methane Emissions and Their Isotopic Signature, Earth System Science Data, 11, 1–22, https://doi.org/10.5194/essd-11-1-2019, 2019.

Fleisher, A. J., Yi, H., Srivastava, A., Polyansky, O. L., Zobov, N. F., and Hodges, J. T.: Absolute ^{13}C/^{12}C Isotope Amount Ratio for Vienna PeeDee Belemnite from Infrared Absorption Spectroscopy, Nature Physics, 17, 889–893, https://doi.org/10.1038/s41567-021-01226-y, 2021.

Ganesan, A. L., Stell, A. C., Gedney, N., Comyn-Platt, E., Hayman, G., Rigby, M., Poulter, B., and Hornibrook, E. R. C.: Spatially Resolved Isotopic Source Signatures of Wetland Methane Emissions, Geophysical Research Letters, 45, 3737–3745, https://doi.org/10.1002/2018GL077536, 2018.

Gromov, S., Brenninkmeijer, C. A. M., and Jöckel, P.: A Very Limited Role of Tropospheric Chlorine as a Sink of the Greenhouse Gas Methane, Atmospheric Chemistry and Physics, 18, 9831–9843, https://doi.org/10.5194/acp-18-9831-2018, 2018.

850 Hmiel, B., Petrenko, V. V., Dyonisius, M. N., Buizert, C., Smith, A. M., Place, P. F., Harth, C., Beaudette, R., Hua, Q., Yang, B., Vimont, I., Michel, S. E., Severinghaus, J. P., Etheridge, D., Bromley, T., Schmitt, J., Faïn, X., Weiss, R. F., and Dlugokencky, E.: Preindustrial $^{14}CH_4$ Indicates Greater Anthropogenic Fossil CH_4 Emissions, Nature, 578, 409–412, https://doi.org/10.1038/s41586-020-1991-8, 2020.

Hooghiemstra, P. B., Krol, M. C., Meirink, J. F., Bergamaschi, P., van der Werf, G. R., Novelli, P. C., Aben, I., and Röckmann, T.: Optimizing Global CO Emission Estimates Using a Four-Dimensional Variational Data Assimilation System and Surface Network Observations,
855 Atmospheric Chemistry and Physics, 11, 4705–4723, https://doi.org/10.5194/acp-11-4705-2011, 2011.

Hossaini, R., Chipperfield, M. P., Saiz-Lopez, A., Fernandez, R., Monks, S., Feng, W., Brauer, P., and von Glasow, R.: A Global Model of Tropospheric Chlorine Chemistry: Organic versus Inorganic Sources and Impact on Methane Oxidation, Journal of Geophysical Research: Atmospheres, 121, 14,214–271,297, https://doi.org/10.1002/2016JD025756, 2016.

Houweling, S., Kaminski, T., Dentener, F., Lelieveld, J., and Heimann, M.: Inverse Modeling of Methane Sources and Sinks Using the Adjoint
860 of a Global Transport Model, Journal of Geophysical Research, 104, 26 137–26 160, https://doi.org/10.1029/1999JD900428, 1999.

Jackson, R. B., Saunois, M., Bousquet, P., Canadell, J. G., Poulter, B., Stavert, A. R., Bergamaschi, P., Niwa, Y., Segers, A., and Tsuruta, A.: Increasing Anthropogenic Methane Emissions Arise Equally from Agricultural and Fossil Fuel Sources, Environmental Research Letters, 15, 71 002–71 002, https://doi.org/10.1088/1748-9326/ab9ed2, 2020.

Janssens-Maenhout, G., Crippa, M., Guizzardi, D., Muntean, M., Schaaf, E., Dentener, F., Bergamaschi, P., Pagliari, V., Olivier, J. G. J.,
865 Peters, J. A. H. W., van Aardenne, J. A., Monni, S., Doering, U., Petrescu, A. M. R., Solazzo, E., and Oreggioni, G. D.: EDGAR v4.3.2 Global Atlas of the Three Major Greenhouse Gas Emissions for the Period 1970–2012, Earth System Science Data, 11, 959–1002, https://doi.org/10.5194/essd-11-959-2019, 2019.

Jöckel, P., Tost, H., Pozzer, A., Brühl, C., Buchholz, J., Ganzeveld, L., Hoor, P., Kerkweg, A., Lawrence, M. G., Sander, R., Steil, B., Stiller, G., Tanarhte, M., Taraborrelli, D., van Aardenne, J., and Lelieveld, J.: The Atmospheric Chemistry General Circulation Model
870 ECHAM5/MESSy1: Consistent Simulation of Ozone from the Surface to the Mesosphere, Atmospheric Chemistry and Physics, 6, 5067–5104, https://doi.org/10.5194/acp-6-5067-2006, 2006.

King, S. L., Quay, P. D., and Lansdown, J. M.: The $^{13}C/^{12}C$ Kinetic Isotope Effect for Soil Oxidation of Methane at Ambient Atmospheric Concentrations, Journal of Geophysical Research: Atmospheres, 94, 18 273–18 277, https://doi.org/10.1029/JD094iD15p18273, 1989.

Krol, M., Houweling, S., Bregman, B., van den Broek, M., Segers, A., van Velthoven, P., Peters, W., Dentener, F., and Bergamaschi, P.: The
875 Two-Way Nested Global Chemistry-Transport Zoom Model TM5: Algorithm and Applications, Atmospheric Chemistry and Physics, 5, 417–432, https://doi.org/10.5194/acp-5-417-2005, 2005.

Krol, M., Peters, W., Hooghiemstra, P., George, M., Clerbaux, C., Hurtmans, D., McInerney, D., Sedano, F., Bergamaschi, P., El Hajj, M., Kaiser, J. W., Fisher, D., Yershov, V., and Muller, J.-P.: How Much CO Was Emitted by the 2010 Fires around Moscow?, Atmospheric Chemistry and Physics, 13, 4737–4747, https://doi.org/10.5194/acp-13-4737-2013, 2013.

880 Lan, X., Basu, S., Schwietzke, S., Bruhwiler, L. M. P., Dlugokencky, E. J., Michel, S. E., Sherwood, O. A., Tans, P. P., Thoning, K., Etiope, G., Zhuang, Q., Liu, L., Oh, Y., Miller, J. B., Pétron, G., Vaughn, B. H., and Crippa, M.: Improved Constraints on Global Methane Emissions and Sinks Using $\delta^{13}C\text{-}CH_4$, Global Biogeochemical Cycles, 35, e2021GB007 000, https://doi.org/10.1029/2021GB007000, 2021.

Lanczos, C.: An Iteration Method for the Solution of the Eigenvalue Problem of Linear Differential and Integral Operators, Journal of Research of the National Bureau of Standards, 45, 255–282, nvlpubs.nist.gov/nistpubs/jres/045/4/V45.N04.A01.pdf, 1950.

885 Lehner, B. and Döll, P.: Development and Validation of a Global Database of Lakes, Reservoirs and Wetlands, Journal of Hydrology, 296, 1–22, https://doi.org/10.1016/j.jhydrol.2004.03.028, 2004.

Liu, L., Zhuang, Q., Oh, Y., Shurpali, N. J., Kim, S., and Poulter, B.: Uncertainty Quantification of Global Net Methane Emissions from Terrestrial Ecosystems Using a Mechanistically Based Biogeochemistry Model, Journal of Geophysical Research: Biogeosciences, 125, e2019JG005 428, https://doi.org/10.1029/2019JG005428, 2020.

890 Ma, J., Kooijmans, L. M. J., Cho, A., Montzka, S. A., Glatthor, N., Worden, J. R., Kuai, L., Atlas, E. L., and Krol, M. C.: Inverse Modelling of Carbonyl Sulfide: Implementation, Evaluation and Implications for the Global Budget, Atmospheric Chemistry and Physics, 21, 3507–3529, https://doi.org/10.5194/acp-21-3507-2021, 2021.

Machida, T., Matsueda, H., Sawa, Y., Nakagawa, Y., Hirotani, K., Kondo, N., Goto, K., Nakazawa, T., Ishikawa, K., and Ogawa, T.: Worldwide Measurements of Atmospheric CO_2 and Other Trace Gas Species Using Commercial Airlines, Journal of Atmospheric and Oceanic
895 Technology, 25, 1744–1754, https://doi.org/10.1175/2008JTECHA1082.1, 2008.

Malinovsky, D., Dunn, P. J. H., Holcombe, G., Cowen, S., and Goenaga-Infante, H.: Development and Characterisation of New Glycine Certified Reference Materials for SI-traceable $^{13}C/^{12}C$ Isotope Amount Ratio Measurements, Journal of Analytical Atomic Spectrometry, 34, 147–159, https://doi.org/10.1039/C8JA00281A, 2019.

Masarie, K. A. and Tans, P. P.: Extension and Integration of Atmospheric Carbon Dioxide Data into a Globally Consistent Measurement
900 Record, Journal of Geophysical Research: Atmospheres, 100, 11 593–11 610, https://doi.org/10.1029/95JD00859, 1995.

Matsueda, H., Machida, T., Sawa, Y., and Niwa, Y.: Long-Term Change of CO_2 Latitudinal Distribution in the Upper Troposphere, Geophysical Research Letters, 42, 2508–2514, https://doi.org/10.1002/2014GL062768, 2015.

Matthews, E. and Fung, I.: Methane Emission from Natural Wetlands: Global Distribution, Area, and Environmental Characteristics of Sources, Global Biogeochemical Cycles, 1, 61–86, https://doi.org/10.1029/GB001i001p00061, 1987.

905 McNorton, J., Wilson, C., Gloor, M., Parker, R. J., Boesch, H., Feng, W., Hossaini, R., and Chipperfield, M. P.: Attribution of Recent Increases in Atmospheric Methane through 3-D Inverse Modelling, Atmospheric Chemistry and Physics, 18, 18 149–18 168, https://doi.org/10.5194/acp-18-18149-2018, 2018.

Meirink, J. F., Bergamaschi, P., and Krol, M. C.: Four-Dimensional Variational Data Assimilation for Inverse Modelling of Atmospheric Methane Emissions: Method and Comparison with Synthesis Inversion, Atmospheric Chemistry and Physics, 8, 6341–6353,
910 https://doi.org/10.5194/acp-8-6341-2008, 2008.

Miller, J. B.: The Carbon Isotopic Composition of Atmospheric Methane and Its Constraint on the Global Methane Budget, in: Stable Isotopes and Biosphere - Atmosphere Interactions, edited by Pataki, D., Ehleringer, J. R., and Flanagan, L. B., pp. 288–310, Academic Press, 1st edn., https://doi.org/10.1016/B978-012088447-6/50016-7, 2004.

Miller, J. B., Mack, K. A., Dissly, R., White, J. W. C., Dlugokencky, E. J., and Tans, P. P.: Development of Analytical Methods and Measure-
915 ments of $^{13}C/^{12}C$ in Atmospheric CH_4 from the NOAA Climate Monitoring and Diagnostics Laboratory Global Air Sampling Network, Journal of Geophysical Research: Atmospheres, 107, ACH 11–1–ACH 11–15, https://doi.org/10.1029/2001JD000630, 2002.

Montzka, S. A., Krol, M., Dlugokencky, E., Hall, B., Jöckel, P., and Lelieveld, J.: Small Interannual Variability of Global Atmospheric Hydroxyl, Science, 331, 67–69, https://doi.org/10.1126/science.1197640, 2011.

Murguia-Flores, F., Ganesan, A. L., Arndt, S., and Hornibrook, E. R. C.: Global Uptake of Atmospheric Methane by Soil from 1900 to 2100,
920 Global Biogeochemical Cycles, 35, e2020GB006 774, https://doi.org/10.1029/2020GB006774, 2021.

Naus, S., Montzka, S. A., Pandey, S., Basu, S., Dlugokencky, E. J., and Krol, M.: Constraints and Biases in a Tropospheric Two-Box Model of OH, Atmospheric Chemistry and Physics, 19, 407–424, https://doi.org/10.5194/acp-19-407-2019, 2019.

Ni, X. and Groffman, P. M.: Declines in Methane Uptake in Forest Soils, Proceedings of the National Academy of Sciences, 115, 8587–8590, https://doi.org/10.1073/pnas.1807377115, 2018.

925 Nicely, J. M., Canty, T. P., Manyin, M., Oman, L. D., Salawitch, R. J., Steenrod, S. D., Strahan, S. E., and Strode, S. A.: Changes in Global Tropospheric OH Expected as a Result of Climate Change Over the Last Several Decades, Journal of Geophysical Research: Atmospheres, 123, 10,774–10,795, https://doi.org/10.1029/2018JD028388, 2018.

Nisbet, E. G., Dlugokencky, E. J., Manning, M. R., Lowry, D., Fisher, R. E., France, J. L., Michel, S. E., Miller, J. B., White, J. W. C., Vaughn, B., Bousquet, P., Pyle, J. A., Warwick, N. J., Cain, M., Brownlow, R., Zazzeri, G., Lanoisellé, M., Manning, A. C., Gloor, E.,

930 Worthy, D. E. J., Brunke, E.-G., Labuschagne, C., Wolff, E. W., and Ganesan, A. L.: Rising Atmospheric Methane: 2007–2014 Growth and Isotopic Shift, Global Biogeochemical Cycles, 30, 1356–1370, https://doi.org/10.1002/2016GB005406, 2016.

Nisbet, E. G., Manning, M. R., Dlugokencky, E. J., Fisher, R. E., Lowry, D., Michel, S. E., Myhre, C. L., Platt, S. M., Allen, G., Bousquet, P., Brownlow, R., Cain, M., France, J. L., Hermansen, O., Hossaini, R., Jones, A. E., Levin, I., Manning, A. C., Myhre, G., Pyle, J. A., Vaughn, B. H., Warwick, N. J., and White, J. W. C.: Very Strong Atmospheric Methane Growth in the 4 Years 2014–2017: Implications

935 for the Paris Agreement, Global Biogeochemical Cycles, 33, 318–342, https://doi.org/10.1029/2018GB006009, 2019.

Oh, Y., Zhuang, Q., Liu, L., Welp, L. R., Lau, M. C. Y., Onstott, T. C., Medvigy, D., Bruhwiler, L., Dlugokencky, E. J., Hugelius, G., D'Imperio, L., and Elberling, B.: Reduced Net Methane Emissions Due to Microbial Methane Oxidation in a Warmer Arctic, Nature Climate Change, 10, 317–321, https://doi.org/10.1038/s41558-020-0734-z, 2020.

Oh, Y., Zhuang, Q., Welp, L. R., Liu, L., Lan, X., Basu, S., Dlugokencky, E. J., Bruhwiler, L., Miller, J. B., Michel, S. E., Schwietzke,

940 S., Tans, P., Ciais, P., and Chanton, J. P.: Improved Global Wetland Carbon Isotopic Signatures Support Post-2006 Microbial Methane Emission Increase, Communications Earth & Environment, 3, 159, https://doi.org/10.1038/s43247-022-00488-5, 2022.

Patra, P. K., Krol, M. C., Montzka, S. A., Arnold, T., Atlas, E. L., Lintner, B. R., Stephens, B. B., Xiang, B., Elkins, J. W., Fraser, P. J., Ghosh, A., Hintsa, E. J., Hurst, D. F., Ishijima, K., Krummel, P. B., Miller, B. R., Miyazaki, K., Moore, F. L., Mühle, J., O'Doherty, S., Prinn, R. G., Steele, L. P., Takigawa, M., Wang, H. J., Weiss, R. F., Wofsy, S. C., and Young, D.: Observational Evidence for Interhemispheric

945 Hydroxyl-Radical Parity, Nature, 513, 219–223, https://doi.org/10.1038/nature13721, 2014.

Patra, P. K., Krol, M. C., Prinn, R. G., Takigawa, M., Mühle, J., Montzka, S. A., Lal, S., Yamashita, Y., Naus, S., Chandra, N., Weiss, R. F., Krummel, P. B., Fraser, P. J., O'Doherty, S., and Elkins, J. W.: Methyl Chloroform Continues to Constrain the Hydroxyl (OH) Variability in the Troposphere, Journal of Geophysical Research: Atmospheres, n/a, e2020JD033 862, https://doi.org/10.1029/2020JD033862, 2020.

Poulter, B., Bousquet, P., Canadell, J. G., Ciais, P., Peregon, A., Saunois, M., Arora, V. K., Beerling, D. J., Brovkin, V., Jones, C. D., Joos,

950 F., Gedney, N., Ito, A., Kleinen, T., Koven, C. D., McDonald, K., Melton, J. R., Peng, C., Peng, S., Prigent, C., Schroeder, R., Riley, W. J., Saito, M., Spahni, R., Tian, H., Taylor, L., Viovy, N., Wilton, D., Wiltshire, A., Xu, X., Zhang, B., Zhang, Z., and Zhu, Q.: Global Wetland Contribution to 2000–2012 Atmospheric Methane Growth Rate Dynamics, Environmental Research Letters, 12, 94 013–94 013, https://doi.org/10.1088/1748-9326/aa8391, 2017.

Quay, P., Stutsman, J., Wilbur, D., Snover, A., Dlugokencky, E., and Brown, T.: The Isotopic Composition of Atmospheric Methane, Global

955 Biogeochemical Cycles, 13, 445–461, https://doi.org/10.1029/1998GB900006, 1999.

Randerson, J. T., Chen, Y., van der Werf, G. R., Rogers, B. M., and Morton, D. C.: Global Burned Area and Biomass Burning Emissions from Small Fires, Journal of Geophysical Research: Biogeosciences, 117, https://doi.org/10.1029/2012JG002128, 2012.

Rice, A. L., Butenhoff, C. L., Teama, D. G., Röger, F. H., Khalil, M. A. K., and Rasmussen, R. A.: Atmospheric Methane Isotopic Record Favors Fossil Sources Flat in 1980s and 1990s with Recent Increase, Proceedings of the National Academy of Sciences, 113, 10 791,

960 https://doi.org/10.1073/pnas.1522923113, 2016.

Rigby, M., Montzka, S. A., Prinn, R. G., White, J. W. C., Young, D., O'Doherty, S., Lunt, M. F., Ganesan, A. L., Manning, A. J., Simmonds, P. G., Salameh, P. K., Harth, C. M., Mühle, J., Weiss, R. F., Fraser, P. J., Steele, L. P., Krummel, P. B., McCulloch, A., and Park, S.: Role of Atmospheric Oxidation in Recent Methane Growth, Proceedings of the National Academy of Sciences, 114, 5373–5377, https://doi.org/10.1073/pnas.1616426114, 2017.

965 Rust, F. and Stevens, C. M.: Carbon Kinetic Isotope Effect in the Oxidation of Methane by Hydroxyl, International Journal of Chemical Kinetics, 12, 371–377, https://doi.org/10.1002/kin.550120602, 1980.

Sanderson, M. G.: Biomass of Termites and Their Emissions of Methane and Carbon Dioxide: A Global Database, Global Biogeochemical Cycles, 10, 543–557, https://doi.org/10.1029/96GB01893, 1996.

Saueressig, G., Crowley, J. N., Bergamaschi, P., Brühl, C., Brenninkmeijer, C. A. M., and Fischer, H.: Carbon-13 and D Kinetic Isotope
970 Effects in the Reactions of CH_4 with $O(^1D)$ and OH: New Laboratory Measurements and Their Implications for the Isotopic Composition of Stratospheric Methane, Journal of Geophysical Research: Atmospheres, 106, 23 127–23 138, https://doi.org/10.1029/2000JD000120, 2001.

Saunois, M., Stavert, A. R., Poulter, B., Bousquet, P., Canadell, J. G., Jackson, R. B., Raymond, P. A., Dlugokencky, E. J., Houweling, S., Patra, P. K., Ciais, P., Arora, V. K., Bastviken, D., Bergamaschi, P., Blake, D. R., Brailsford, G., Bruhwiler, L., Carlson, K. M., Carrol,
975 M., Castaldi, S., Chandra, N., Crevoisier, C., Crill, P. M., Covey, K., Curry, C. L., Etiope, G., Frankenberg, C., Gedney, N., Hegglin, M. I., Höglund-Isaksson, L., Hugelius, G., Ishizawa, M., Ito, A., Janssens-Maenhout, G., Jensen, K. M., Joos, F., Kleinen, T., Krummel, P. B., Langenfelds, R. L., Laruelle, G. G., Liu, L., Machida, T., Maksyutov, S., McDonald, K. C., McNorton, J., Miller, P. A., Melton, J. R., Morino, I., Müller, J., Murguia-Flores, F., Naik, V., Niwa, Y., Noce, S., O'Doherty, S., Parker, R. J., Peng, C., Peng, S., Peters, G. P., Prigent, C., Prinn, R., Ramonet, M., Regnier, P., Riley, W. J., Rosentreter, J. A., Segers, A., Simpson, I. J., Shi, H., Smith, S. J., Steele, L. P.,
980 Thornton, B. F., Tian, H., Tohjima, Y., Tubiello, F. N., Tsuruta, A., Viovy, N., Voulgarakis, A., Weber, T. S., van Weele, M., van der Werf, G. R., Weiss, R. F., Worthy, D., Wunch, D., Yin, Y., Yoshida, Y., Zhang, W., Zhang, Z., Zhao, Y., Zheng, B., Zhu, Q., Zhu, Q., and Zhuang, Q.: The Global Methane Budget 2000–2017, Earth System Science Data, 12, 1561–1623, https://doi.org/10.5194/essd-12-1561-2020, 2020.

Schaefer, H., Fletcher, S. E. M., Veidt, C., Lassey, K. R., Brailsford, G. W., Bromley, T. M., Dlugokencky, E. J., Michel, S. E., Miller, J. B.,
985 Levin, I., Lowe, D. C., Martin, R. J., Vaughn, B. H., and White, J. W. C.: A 21st Century Shift from Fossil-Fuel to Biogenic Methane Emissions Indicated by $^{13}CH_4$, Science, https://doi.org/10.1126/science.aad2705, 2016.

Schroeder, R., McDonald, K. C., Chapman, B. D., Jensen, K., Podest, E., Tessler, Z. D., Bohn, T. J., and Zimmermann, R.: Development and Evaluation of a Multi-Year Fractional Surface Water Data Set Derived from Active/Passive Microwave Remote Sensing Data, Remote Sensing, 7, 16 688–16 732, https://doi.org/10.3390/rs71215843, 2015.

990 Schultz, M. G., Heil, A., Hoelzemann, J. J., Spessa, A., Thonicke, K., Goldammer, J. G., Held, A. C., Pereira, J. M. C., and van het Bolscher, M.: Global Wildland Fire Emissions from 1960 to 2000, Global Biogeochemical Cycles, 22, https://doi.org/10.1029/2007GB003031, 2008.

Schwietzke, S., Sherwood, O. A., Bruhwiler, L. M. P., Miller, J. B., Etiope, G., Dlugokencky, E. J., Michel, S. E., Arling, V. A., Vaughn, B. H., White, J. W. C., and Tans, P. P.: Upward Revision of Global Fossil Fuel Methane Emissions Based on Isotope Database, Nature,
995 538, 88–91, https://doi.org/10.1038/nature19797, 2016.

Sherwood, O. A., Schwietzke, S., and Lan, X.: Global Inventory of Fossil and Non-fossil δ^{13}C-CH_4 Source Signature Measurements for Improved Atmospheric Modeling, https://doi.org/10.15138/qn55-e011, 2021.

Sowers, T.: Late Quaternary Atmospheric CH_4 Isotope Record Suggests Marine Clathrates Are Stable, Science, 311, 838–840, https://doi.org/10.1126/science.1121235, 2006.

1000   Spivakovsky, C. M., Logan, J. A., Montzka, S. A., Balkanski, Y. J., Foreman-Fowler, M., Jones, D. B. A., Horowitz, L. W., Fusco, A. C., Brenninkmeijer, C. A. M., Prather, M. J., Wofsy, S. C., and McElroy, M. B.: Three-Dimensional Climatological Distribution of Tropospheric OH: Update and Evaluation, Journal of Geophysical Research: Atmospheres, 105, 8931–8980, https://doi.org/10.1029/1999JD901006, 2000.

Steil, B., Brühl, C., Manzini, E., Crutzen, P. J., Lelieveld, J., Rasch, P. J., Roeckner, E., and Krüger, K.: A New Interactive Chemistry-Climate
1005   Model: 1. Present-day Climatology and Interannual Variability of the Middle Atmosphere Using the Model and 9 Years of HALOE/UARS Data, Journal of Geophysical Research: Atmospheres, 108, https://doi.org/10.1029/2002JD002971, 2003.

Still, C. J., Berry, J. A., Collatz, G. J., and DeFries, R. S.: Global Distribution of C3 and C4 Vegetation: Carbon Cycle Implications, Global Biogeochemical Cycles, 17, 6–1–6–14, https://doi.org/10.1029/2001GB001807, 2003.

Strode, S. A., Wang, J. S., Manyin, M., Duncan, B., Hossaini, R., Keller, C. A., Michel, S. E., and White, J. W. C.: Strong Sensitivity of the
1010   Isotopic Composition of Methane to the Plausible Range of Tropospheric Chlorine, Atmospheric Chemistry and Physics, 20, 8405–8419, https://doi.org/10.5194/acp-20-8405-2020, 2020.

Sweeney, C., Karion, A., Wolter, S., Newberger, T., Guenther, D., Higgs, J. A., Andrews, A. E., Lang, P. M., Neff, D., Dlugokencky, E., Miller, J. B., Montzka, S. A., Miller, B. R., Masarie, K. A., Biraud, S. C., Novelli, P. C., Crotwell, M., Crotwell, A. M., Thoning, K., and Tans, P. P.: Seasonal Climatology of CO_2 across North America from Aircraft Measurements in the NOAA/ESRL Global Greenhouse Gas
1015   Reference Network, Journal of Geophysical Research: Atmospheres, 120, 5155–5190, https://doi.org/10.1002/2014JD022591, 2015.

Tans, P. P.: A Note on Isotopic Ratios and the Global Atmospheric Methane Budget, Global Biogeochemical Cycles, 11, 77–81, https://doi.org/10.1029/96GB03940, 1997.

Tans, P. P., Berry, J. A., and Keeling, R. F.: Oceanic $^{13}C/^{12}C$ Observations: A New Window on Ocean CO_2 Uptake, Global Biogeochemical Cycles, 7, 353–368, https://doi.org/10.1029/93GB00053, 1993.

1020   Thanwerdas, J., Saunois, M., Berchet, A., Pison, I., Vaughn, B. H., Michel, S. E., and Bousquet, P.: Variational Inverse Modelling within the Community Inversion Framework to Assimilate $\delta^{13}C(CH_4)$ and CH_4: A Case Study with Model LMDz-SACS, Geoscientific Model Development Discussions, 2021, 1–29, https://doi.org/10.5194/gmd-2021-106, 2021.

Thompson, C. R., Wofsy, S. C., Prather, M. J., Newman, P. A., Hanisco, T. F., Ryerson, T. B., Fahey, D. W., Apel, E. C., Brock, C. A., Brune, W. H., Froyd, K., Katich, J. M., Nicely, J. M., Peischl, J., Ray, E., Veres, P. R., Wang, S., Allen, H. M., Asher, E., Bian, H., Blake,
1025   D., Bourgeois, I., Budney, J., Bui, T. P., Butler, A., Campuzano-Jost, P., Chang, C., Chin, M., Commane, R., Correa, G., Crounse, J. D., Daube, B., Dibb, J. E., DiGangi, J. P., Diskin, G. S., Dollner, M., Elkins, J. W., Fiore, A. M., Flynn, C. M., Guo, H., Hall, S. R., Hannun, R. A., Hills, A., Hintsa, E. J., Hodzic, A., Hornbrook, R. S., Huey, L. G., Jimenez, J. L., Keeling, R. F., Kim, M. J., Kupc, A., Lacey, F., Lait, L. R., Lamarque, J.-F., Liu, J., McKain, K., Meinardi, S., Miller, D. O., Montzka, S. A., Moore, F. L., Morgan, E. J., Murphy, D. M., Murray, L. T., Nault, B. A., Neuman, J. A., Nguyen, L., Gonzalez, Y., Rollins, A., Rosenlof, K., Sargent, M., Schill, G., Schwarz,
1030   J. P., Clair, J. M. S., Steenrod, S. D., Stephens, B. B., Strahan, S. E., Strode, S. A., Sweeney, C., Thames, A. B., Ullmann, K., Wagner, N., Weber, R., Weinzierl, B., Wennberg, P. O., Williamson, C. J., Wolfe, G. M., and Zeng, L.: The NASA Atmospheric Tomography (ATom) Mission: Imaging the Chemistry of the Global Atmosphere, Bulletin of the American Meteorological Society, 103, E761 – E790, https://doi.org/10.1175/BAMS-D-20-0315.1, 2022.

Thompson, R. L., Nisbet, E. G., Pisso, I., Stohl, A., Blake, D., Dlugokencky, E. J., Helmig, D., and White, J. W. C.: Variability in Atmospheric Methane from Fossil Fuel and Microbial Sources over the Last Three Decades, Geophysical Research Letters, 45, 11,499–11,508, https://doi.org/10.1029/2018GL078127, 2018.

Thoning, K. W., Tans, P. P., and Komhyr, W. D.: Atmospheric Carbon Dioxide at Mauna Loa Observatory 2. Analysis of the NOAA GMCC Data, 1974–1985, Journal of Geophysical Research, 94, 8549–8565, https://doi.org/10.1029/JD094iD06p08549, 1989.

Turner, A. J., Frankenberg, C., Wennberg, P. O., and Jacob, D. J.: Ambiguity in the Causes for Decadal Trends in Atmospheric Methane and Hydroxyl, Proceedings of the National Academy of Sciences, 114, 5367–5372, https://doi.org/10.1073/pnas.1616020114, 2017.

Umezawa, T., Machida, T., Ishijima, K., Matsueda, H., Sawa, Y., Patra, P. K., Aoki, S., and Nakazawa, T.: Carbon and Hydrogen Isotopic Ratios of Atmospheric Methane in the Upper Troposphere over the Western Pacific, Atmospheric Chemistry and Physics, 12, 8095–8113, https://doi.org/10.5194/acp-12-8095-2012, 2012.

Umezawa, T., Brenninkmeijer, C. A. M., Röckmann, T., van der Veen, C., Tyler, S. C., Fujita, R., Morimoto, S., Aoki, S., Sowers, T., Schmitt, J., Bock, M., Beck, J., Fischer, H., Michel, S. E., Vaughn, B. H., Miller, J. B., White, J. W. C., Brailsford, G., Schaefer, H., Sperlich, P., Brand, W. A., Rothe, M., Blunier, T., Lowry, D., Fisher, R. E., Nisbet, E. G., Rice, A. L., Bergamaschi, P., Veidt, C., and Levin, I.: Interlaboratory Comparison of δ^{13}C and δD Measurements of Atmospheric CH$_4$ for Combined Use of Data Sets from Different Laboratories, Atmospheric Measurement Techniques, 11, 1207–1231, https://doi.org/10.5194/amt-11-1207-2018, 2018.

van der Werf, G. R., Randerson, J. T., Giglio, L., van Leeuwen, T. T., Chen, Y., Rogers, B. M., Mu, M., van Marle, M. J. E., Morton, D. C., Collatz, G. J., Yokelson, R. J., and Kasibhatla, P. S.: Global Fire Emissions Estimates during 1997–2016, Earth System Science Data, 9, 697–720, https://doi.org/10.5194/essd-9-697-2017, 2017.

Wang, X., Jacob, D. J., Downs, W., Zhai, S., Zhu, L., Shah, V., Holmes, C. D., Sherwen, T., Alexander, B., Evans, M. J., Eastham, S. D., Neuman, J. A., Veres, P., Koenig, T. K., Volkamer, R., Huey, L. G., Bannan, T. J., Percival, C. J., Lee, B. H., and Thornton, J. A.: Global Tropospheric Halogen (Cl, Br, I) Chemistry and Its Impact on Oxidants, Atmospheric Chemistry and Physics Discussions, 2021, 1–34, https://doi.org/10.5194/acp-2021-441, 2021.

Whitehill, A. R., Joelsson, L. M. T., Schmidt, J. A., Wang, D. T., Johnson, M. S., and Ono, S.: Clumped Isotope Effects during OH and Cl Oxidation of Methane, Geochimica et Cosmochimica Acta, 196, 307–325, https://doi.org/10.1016/j.gca.2016.09.012, 2017.

Whiticar, M. and Schaefer, H.: Constraining Past Global Tropospheric Methane Budgets with Carbon and Hydrogen Isotope Ratios in Ice, Philosophical Transactions of the Royal Society A: Mathematical, Physical and Engineering Sciences, 365, 1793–1828, https://doi.org/10.1098/rsta.2007.2048, 2007.

Wofsy, S. C.: HIAPER Pole-to-Pole Observations (HIPPO): Fine-Grained, Global-Scale Measurements of Climatically Important Atmospheric Gases and Aerosols, Philosophical Transactions of the Royal Society A: Mathematical, Physical and Engineering Sciences, 369, 2073–2086, https://doi.org/10.1098/rsta.2010.0313, 2011.

Worden, J. R., Bloom, A. A., Pandey, S., Jiang, Z., Worden, H. M., Walker, T. W., Houweling, S., and Röckmann, T.: Reduced Biomass Burning Emissions Reconcile Conflicting Estimates of the Post-2006 Atmospheric Methane Budget, Nature Communications, 8, 2227–2227, https://doi.org/10.1038/s41467-017-02246-0, 2017.

Yin, Y., Chevallier, F., Ciais, P., Bousquet, P., Saunois, M., Zheng, B., Worden, J., Bloom, A. A., Parker, R. J., Jacob, D. J., Dlugokencky, E. J., and Frankenberg, C.: Accelerating Methane Growth Rate from 2010 to 2017: Leading Contributions from the Tropics and East Asia, Atmospheric Chemistry and Physics, 21, 12 631–12 647, https://doi.org/10.5194/acp-21-12631-2021, 2021.

Zhang, Q.-L. and Li, W.-J.: A Calibrated Measurement of the Atomic Weight of Carbon, Chinese Science Bulletin, 35, 290–296, https://doi.org/10.1360/sb1990-35-4-290, 1990.

Zhang, Y., Jacob, D. J., Maasakkers, J. D., Sulprizio, M. P., Sheng, J.-X., Gautam, R., and Worden, J.: Monitoring Global Tropospheric OH Concentrations Using Satellite Observations of Atmospheric Methane, Atmospheric Chemistry and Physics, 18, 15 959–15 973, https://doi.org/10.5194/acp-18-15959-2018, 2018.

1075 Zhang, Y., Jacob, D. J., Lu, X., Maasakkers, J. D., Scarpelli, T. R., Sheng, J.-X., Shen, L., Qu, Z., Sulprizio, M. P., Chang, J., Bloom, A. A., Ma, S., Worden, J., Parker, R. J., and Boesch, H.: Attribution of the Accelerating Increase in Atmospheric Methane during 2010–2018 by Inverse Analysis of GOSAT Observations, Atmospheric Chemistry and Physics, 21, 3643–3666, https://doi.org/10.5194/acp-21-3643-2021, 2021a.

Zhang, Z., Poulter, B., Knox, S., Stavert, A., McNicol, G., Fluet-Chouinard, E., Feinberg, A., Zhao, Y., Bousquet, P., Canadell, J. G.,

1080 Ganesan, A., Hugelius, G., Hurtt, G., Jackson, R. B., Patra, P. K., Saunois, M., Höglund-Isaksson, L., Huang, C., Chatterjee, A., and Li, X.: Anthropogenic Emission Is the Main Contributor to the Rise of Atmospheric Methane during 1993–2017, National Science Review, 9, https://doi.org/10.1093/nsr/nwab200, 2021b.

Zhuang, Q., Melillo, J. M., Kicklighter, D. W., Prinn, R. G., McGuire, A. D., Steudler, P. A., Felzer, B. S., and Hu, S.: Methane Fluxes between Terrestrial Ecosystems and the Atmosphere at Northern High Latitudes during the Past Century: A Retrospective Analysis with

1085 a Process-Based Biogeochemistry Model, Global Biogeochemical Cycles, 18, https://doi.org/10.1029/2004GB002239, 2004.